Composites: Part A 207 (2026) 109829

Contents lists available at ScienceDirect

Composites Part A

journal homepage: www.elsevier.com/locate/compositesa

MoS_2 and PTFE, two competitive high performance dry lubricants for carbon fiber reinforced PPS in hydrogen compression applications

Alexander Pöllinger [a,b,*,1], Julia Thalhammer [c], Sarah Heupl [c], Fabian Wilde [d], Gábor Szakács [d], Stefan Krenn [e], Klaus Gebhardt [f], Eleni Siakkou [f], Thomas Koch [a], Vasiliki-Maria Archodoulaki [a], Michael Schöbel [g,h,2]

[a] Institute of Materials Science and Technology, TU Wien, Getreidemarkt 9, Vienna, 1060, Austria
[b] Leobersdorfer Maschinenfabrik GmbH, Südbahnstraße 28, Leobersdorf, 2544, Austria
[c] University of Applied Sciences Upper Austria, Stelzhamerstraße 23, Wels, 4600, Austria
[d] Helmholtz-Zentrum Hereon, Max–Planck-Straße 1, Geesthacht, 21502, Germany
[e] AC2T research GmbH, Viktor-Kaplan-Straße 2/C, Wiener Neustadt, 2700, Austria
[f] MOCOM Compounds GmbH & Co. KG, Mühlenhagen 35, Hamburg, 20539, Germany
[g] TAG GmbH, Wienerbergstraße 11, Vienna, 1100, Austria
[h] X-ray Center, TU Wien, Getreidemarkt 9, Vienna, 1060, Austria

ARTICLE INFO

Keywords:
Polymer-matrix composites
Synchrotron tomography
Tribology
Mechanical testing
Hydrogen

ABSTRACT

Efficient hydrogen compression is a critical component for the transition to renewable energy systems. High-pressure reciprocating piston compressors require advanced tribological solutions to ensure durability, reliability, and gas purity under dry-running conditions. Polyphenylene sulfide (PPS) polymer matrix composites, known for their excellent mechanical and thermal stability, are currently of high interest in research. This study compares the performance of molybdenum disulfide (MoS_2) and polytetrafluoroethylene (PTFE) as dry lubricants for PPS-based piston ring materials in high-pressure hydrogen environments. This work utilizes tribological and thermo-mechanical testing, along with microstructural analysis, to systematically evaluate the effects of these lubricants on friction, wear, and load-bearing capacity. Advanced imaging techniques, including synchrotron tomography, reveal the role of lubricant dispersion and interaction with PPS. The findings highlight key differences in the tribological performance of MoS_2 and PTFE, offering insights into their suitability for high-pressure hydrogen compressor applications. This research identifies promising material combinations that will significantly improve the reliability and efficiency of hydrogen compression.

1. Introduction

Under the Paris Agreement signed in 2015, many countries committed to significantly reducing anthropogenic greenhouse gas emissions to limit global warming to 2 °C by the second half of this century [1]. Renewable energy sources, such as wind turbines and solar panels, offer promising solutions to achieve this goal. However, their energy generation is inherently intermittent as it is influenced by weather conditions, time of day, and seasonal variations. To address these challenges, gaseous hydrogen could be a viable alternative to replace a substantial portion of current fossil primary energy sources. Its compatibility with existing infrastructure and capacity for long-term storage make it a key technology in a carbon-neutral energy system [2–5].

Hydrogen produced with water electrolysis typically has an output pressure ranging from 1 bar to 30 bar. However, for practical use in transportation applications, gaseous hydrogen must be compressed to pressures that exceed 500 bar to achieve a sufficient volumetric energy density. As a result, hydrogen compressor stations play a critical role in hydrogen infrastructure, compressing hydrogen from its initial low pressure to high pressures and enabling efficient storage in high-pressure tanks in fuel cell electric vehicles. Given that compressors contribute around 54 % of the capital expenditure of a hydrogen refueling station, the demand for reliable and efficient high-pressure compressor solutions continues to rise [6]. Currently, diaphragm, hydraulic drive piston, or ionic liquid compressors are used, but these are

* Corresponding author at: Leobersdorfer Maschinenfabrik GmbH, Südbahnstraße 28, Leobersdorf, 2544, Austria.
E-mail addresses: alexander.poellinger@lmf.at (A. Pöllinger), michael.schoebel@tuwien.ac.at (M. Schöbel).
URL: https://www.lmf.at (A. Pöllinger).
[1] Researcher
[2] Coordinator

https://doi.org/10.1016/j.compositesa.2026.109829
Received 18 December 2025; Received in revised form 28 March 2026; Accepted 10 April 2026
Available online 14 April 2026

limited in efficiency due to low volume flow rates, high maintenance costs, and short service intervals [2,7,8].

An alternative to state-of-the-art compression systems is the crank-driven reciprocating piston compressor, which is capable of achieving both high discharge pressures and substantial pressure ratios. This type of compressor is widely considered the industry standard for oil-lubricated applications at pressures of up to 250 bar [9]. Non-lubricated compressor designs, necessary to supply hydrogen according to established gas quality standards, including ISO 14687:2025, SAE J2719:2020, and EN 17124:2022, do not achieve sufficient discharge pressures suitable for transport applications (>500 bar) [10–12].

The primary limitation of non-lubricated reciprocating compressors arises from the sealing elements between the piston and the cylinder liner. In hydrogen reciprocating compressors, the sealing system typically consists of multiple slotted piston rings with a defined circumferential gap. This gap is an inherent design feature required for installation, thermal expansion as well as limiting the pressure load on a single ring. As a consequence, a small and continuous blow-by flow across the ring cannot be completely avoided and is, to some extent, functionally accepted. The piston ring therefore does not provide a hermetic seal. Instead, it acts as a dynamic throttling element that reduces the pressure gradient in a staged manner while maintaining compressor efficiency and homogeneous ring pressure distribution. The rings are subjected to complex multi-axial stress states due to pressure gradients and frictional forces while simultaneously being optimized for tribological performance [13]. Consequently, a major research challenge lies in designing sealing systems that not only provide effective performance, but also enable long maintenance intervals.

State-of-the-art reciprocating compressor piston rings commonly utilize polytetrafluoroethylene (PTFE) piston rings, manufactured by injection molding or machining from sintered blanks. To enhance structural integrity and improve the wear resistance of the parts, they are often reinforced with carbon fibers [14–16]. However, in high-pressure hydrogen applications, conventional material combinations impose limitations, as excessive thermo-mechanical stresses can lead to critical failures such as ring extrusion, accelerated wear, or thermal degradation [17]. As a result, ensuring adequate piston ring longevity and maintaining compressor performance under extreme operating conditions present a significant materials science challenge. To address these limitations, research has recently focused on high-performance polymers, including polyetheretherketone (PEEK), polyimide (PI), and polyphenylene sulfide (PPS) [18–25].

PPS polymer composites exhibit good thermal stability, high strength, and chemical resistance against various atmospheres, including hydrogen [26–30]. PPS has been shown to be a versatile material and can be found in a wide range of applications including electronics, electrical devices, vehicle parts, and aerospace components [31–33]. Recent contributions have investigated the applicability of PPS in reciprocating compressor sealing systems [24,25]. Although a promising material candidate, carbon fiber reinforced PPS exhibits high friction coefficients and wear, but the addition of solid lubricants such as PTFE can significantly improve the tribological performance of fiber reinforced polymers [34–37]. This can be attributed to the sensitivity of the metal–polymer tribo-pair performance to the growth of a protective film on the surface of the metal counterpart. This effect can reduce friction and improve the wear resistance of polymers by preventing direct contact with the counter surface and is one of the main mechanisms that define the excellent tribological properties of PTFE [38]. Recent contributions support this, investigating the applicability of PPS in reciprocating hydrogen compressor sealing systems, indicating that a lubricating component is needed to ensure the formation of a tribo-film [25,39,40].

In 2020, the European Chemicals Agency (ECHA), through the EU Chemicals Strategy for Sustainability, has proposed a gradual ban and phase-out of all per- and polyfluorinated alkyl substances (PFAS), which would include PTFE [41]. This poses a significant challenge for industries that rely on PTFE, particularly in applications such as reciprocating compressor piston rings [14–16]. Given the difficulty of finding direct replacements with comparable properties, this study investigates the potential of carbon fiber reinforced PPS composites with molybdenum disulfide (MoS_2) as an alternative dry lubricant. By comparing the tribological behavior and thermal performance of PPS-based composites to PTFE, this work aims to assess their feasibility in high-performance applications requiring low friction and high wear resistance.

There is a literature gap on short fiber-reinforced PPS matrix composites containing MoS_2, which have not been extensively studied. This research aims to close that gap by investigating the thermo-mechanical properties and microstructural effects on the wear resistance of three experimental PPS matrix composites. Specifically, the influence of varying MoS_2 fractions in comparison to a reference material lubricated with PTFE is examined, assessing the feasibility of MoS_2-lubricated PPS composites for high-pressure hydrogen compression applications. The study focuses on evaluating the tribological performance, deformation behavior, and crack growth mechanisms of these composites as a function of MoS_2 content. Advanced imaging techniques and Digital Volume Correlation (DVC) are employed to track and analyze the material's load response, providing insight into the initiation and propagation of defects. This approach enables a detailed assessment of microstructural deformation patterns, offering a deeper understanding of the mechanical performance of carbon fiber reinforced PPS.

Table 1
Material composition of the injection molded PPS composite test specimen and Böhler W360 metal counterparts for tribological testing.

Abbreviated form	PPS (wt.%)	MoS_2 (wt.%)	PTFE (wt.%)	CF (wt.%)
PPS10PTFE/CF32f	58	–	10	32
PPS2MoS_2/CF32f	66	2	–	32
PPS5MoS_2/CF32f	63	5	–	32

Böhler W360 (wt.%): Fe 90.95, C 0.50, Si 0.20, Mn 0.25, Cr 4.5, Mo 3.0, V 0.6.

2. Materials and methods

2.1. Test materials

Rectangular sample plates ($80 \times 80 \times 3\,mm^3$) were produced from experimental PPS compounds reinforced with 32 wt.% carbon fiber (CF), supplied by MOCOM Compounds GmbH & Co. KG (Hamburg, Germany). Before injection molding, the granulated materials were pre-dried in a dry-air dryer at 130 °C to 140 °C for a duration of 2 h to 4 h. During molding, the polymer melt temperature was maintained between 320 °C to 340 °C, while the mold temperature was kept below 140 °C. The resulting fiber orientation within this plaque geometry, previously characterized for these process parameters, is shown in Fig. 1(a) [24].

In this study, three PPS compounds were investigated, all containing chopped CF reinforcement at a constant mass fraction of 32 wt.%. A reference formulation, PPS10PTFE/CF32f, contained PTFE as a solid lubricant based on its favorable tribological and mechanical performance reported in earlier studies [25]. The other two formulations, PPS2MoS_2/CF32f and PPS5MoS_2/CF32f, incorporated 2 wt.% and 5 wt.% MoS_2 as lubricant additive, respectively. The composition of all three PPS compounds is summarized in Table 1.

The neat PPS matrix is characterized by a Young's modulus of approximately 4 GPa, an ultimate tensile strength ranging from 30 MPa to 90 MPa, and a coefficient of linear thermal expansion (CTE) of approximately 50 ppm/K. Its density is $1.35\,g/cm^3$. Carbon fiber reinforcement, consisting of chopped filaments with a diameter of 7 µm and a nominal length of 6 mm, has a single-filament tensile strength of 4.0 GPa, a modulus of 240 GPa and a density of $1.8\,g/cm^3$. No additional surface treatments were applied to the fibers. The PTFE powder used as a lubricant exhibited an average particle size of 12 µm, a density

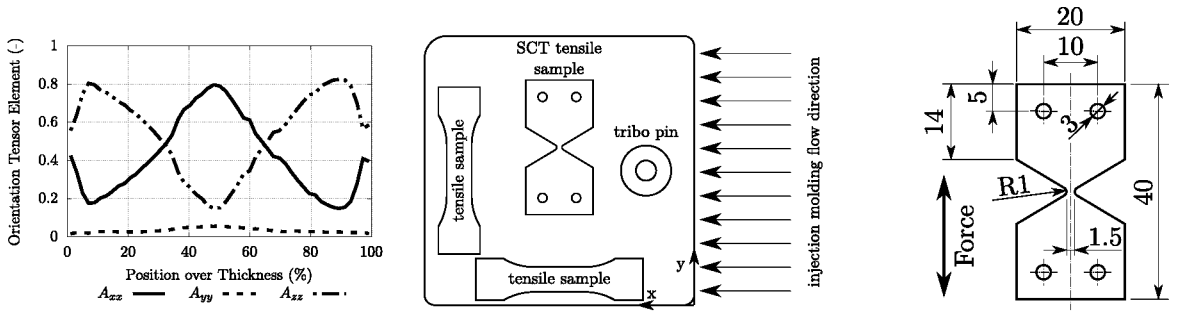

(a) Fiber orientation. (b) Test sample orientation. (c) Tensile testing geometry.

Fig. 1. Test samples, fiber orientation distribution in the sample plaques adapted from [24] (a), orientation of the tensile test and tribology testing samples in the injection molded sample plate in relation to injection molding flow direction (b), specimen geometry for in-situ tensile testing during synchrotron tomography (c).

Table 2
Mechanical properties of the PPS matrix and blend components used in the composite.

Constituent	Density (g/cm^3)	E-Modulus (GPa)
PPS	1.35	4
MoS_2	4.8	240
PTFE	2.15	0.5
CF	1.8	240

of 2.15 g/cm^3, and a Young's modulus of 0.5 GPa. The MoS_2 particles used in this study had a mean diameter of approximately 6 µm and a density of 4.8 g/cm^3. The Young's modulus of bulk MoS_2 is approximately 240 GPa [42]. The CF content was kept constant throughout all formulations, and adjustments were made to the total PPS matrix content to accommodate the additional lubricant mass. A summary of the properties of the components is provided in Table 2.

Compounding of all formulations was performed at MOCOM using a co-rotating twin-screw extruder equipped with a strand pelletization system. The process parameters were uniformly applied to all compositions. To minimize the risk of lubricant agglomeration at the targeted filler content, PTFE and MoS_2 additives were introduced both before and after CF, following strategies suggested in the literature [43]. The extrusion temperature profile was carefully managed to balance melt viscosity and shear input, while pressure build-up zones and die design were optimized to minimize excessive shear forces that could degrade PTFE or shorten CF lengths. The screw configuration also incorporated degassing sections and pressure building elements to ensure stable melt pressure and effective removal of volatiles.

2.2. Tribometry

To achieve an accurate simulation of the mechanical loading conditions acting on a typical piston ring arrangement, a pin-on-plate test configuration was used for the tribological characterization of the PPS matrix composites. The experiments were conducted using a custom-designed reciprocating tribometer, referred to as LOTuGA (**L**inear **O**scillating **T**ribometer **u**nder **G**as **A**tmosphere), at AC2T research GmbH (Wiener Neustadt, Austria). A schematic of the experimental setup is shown in Fig. 2.

The LOTuGA tribometer utilizes a mechanical crank mechanism, derived from a commercially available compressor system, to convert the rotational motion of the electric drive into a linear reciprocating oscillation. This mechanism generates a stroke of 90 mm, resulting in a total sliding distance of 180 mm per cycle at an operating speed of 330 rpm, corresponding to an average sliding velocity of approximately 1 m/s.

A constant nominal contact pressure of 16 MPa, calculated on the basis of service conditions, was applied to two oppositely oriented PPS polymer pins using a pneumatic actuator. The metallic counter samples (plates) were mounted on the oscillating sample holder as shown in Fig. 2(b). Although this configuration is inverted compared to the ring-and-cylinder geometry in the target application, it facilitates direct access to the polymer pins for in situ temperature measurements. The metallic counterparts were water-cooled through internal channels in the sample holder, employing a cooling configuration and power comparable to those used in high-pressure hydrogen reciprocating compressor systems.

Friction and wear behavior were investigated using cylindrical pins with a diameter of 6 mm and an allowable wear depth of 1.5 mm. The specimens were CNC-machined from the central region of injection-molded plates, as illustrated in Fig. 1(b), to ensure uniform material properties among all test samples.

The metallic counter bodies were produced from annealed Böhler W360 hot-work tool steel [44], selected for its high abrasion resistance. Their surfaces were ground perpendicular to the sliding direction to a roughness of $R_a = 0.15 \pm 0.01$ µm, replicating the surface texture of reciprocating compressor cylinder liners used in hydrogen compressor applications. The chemical composition of the W360 steel is provided in Table 1.

To reproduce representative operating conditions of a dry, oxygen- and humidity-free hydrogen environment, a specific gas flushing protocol was applied. At the beginning of each test, the chamber was purged with high-purity nitrogen gas (N5.0 N_2) for two minutes, displacing residual oxygen. During the main test phase under loaded sliding, the chamber was continuously flushed with purity grade 5.0 hydrogen gas, and upon completion of the test run, the chamber was purged with nitrogen for two minutes to safely remove residual hydrogen.

Each experiment was conducted for 20 000 cycles (except PPS2MoS_2/CF32f, which had to be stopped manually earlier due to excessive wear), corresponding to a total sliding distance of approximately 3600 m. This test duration was selected to ensure the stabilization of transient effects such as running-in behavior and tribo-film formation.

The friction force acting on the pins was continuously measured throughout the experiment and the coefficient of friction (CoF) was calculated accordingly. Wear was determined by measuring the displacement of the pin sample holder during the testing, corresponding to the reduction in pin height. The validation of the wear data was performed by focus-variation 3D microscopy using an Alicona InfiniteFocus system before and after each test to quantify the wear volume by differential topography analysis.

The temperature of the polymer pins was measured using thermocouples inserted from the rear side, positioned approximately 3 mm from the sliding interface. The temperature of the metallic counter sample plates was determined by infrared thermography.

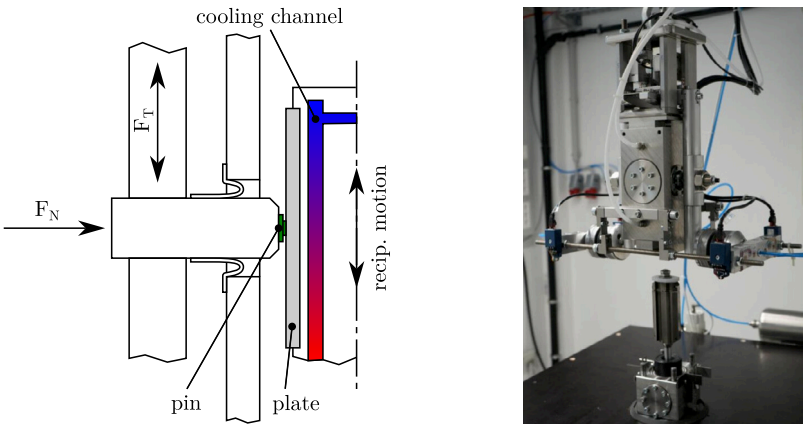

(a) Tribology test setup. (b) Tribometer test cell.

Fig. 2. Tribology, tribometer test setup schematic of the pin on plate test showing the cooling of the metallic counterparts (a), overview of the tribometer with opened test cell (b).

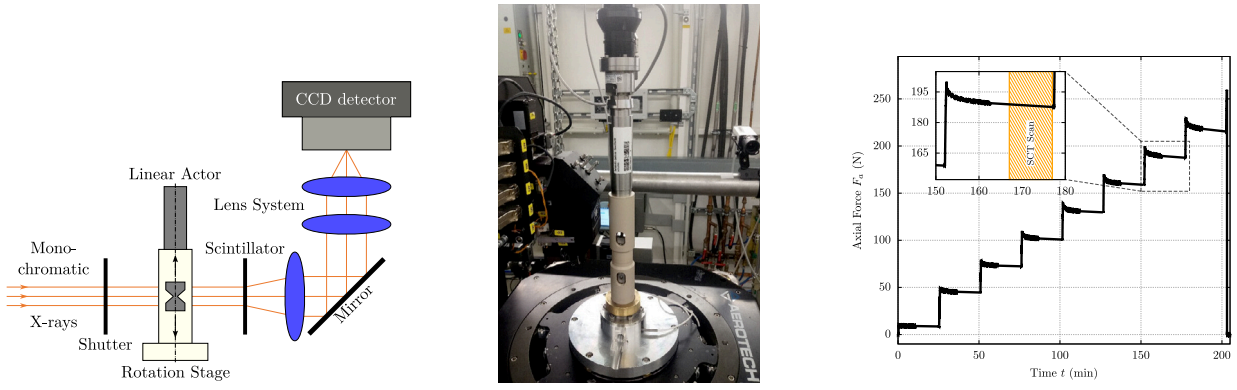

(a) SCT setup. (b) Assembled test setup. (c) Tensile load profile.

Fig. 3. SCT, Schematic drawing of SCT tomography and in-situ tensile test setup (a), assembled measurement setup on P05 beamline at PETRA3 (b) and representative measured tensile test load profile (c).

2.3. Imaging

In-situ synchrotron X-ray computed tomography (SCT) combined with tensile testing was carried out at beamline P05 of the PETRA III synchrotron facility operated by Helmholtz-Zentrum Hereon in Hamburg, Germany. The imaging was performed using a monochromatic parallel beam at 15 keV, chosen to optimize the contrast between the PPS matrix and the carbon fibers, which exhibit similar absorption coefficients. The measurement volume was limited to 2.5×2.5×2.5 mm^3. The projection images were acquired with a Ximea CB500MG camera equipped with a CMOSIS CMV50000 CCD sensor (5120×3840 px^2, 6.5 µm pixel size). The sample-to-detector distance was set to 60 mm to balance phase and absorption contrast. An overview of the test setup is shown in Fig. 3(a).

Each scan consisted of 3000 projections acquired during a continuous 360° rotation over approximately 13 min (250 ms per projection), with data recorded in binning-2 mode. The specimens, with a maximum cross-section of 1.8 × 1.8 mm^2, were fully penetrated by the beam.

The experimental setup depicted in Fig. 3(b) incorporated a custom-designed tensile stage mounted within the beamline load frame infrastructure [45]. Tensile loading followed a stepwise procedure based on the methodology introduced by Maurer et al. [46]. The axial load was increased in discrete increments of 30 N, approximately 10 % of the estimated tensile strength of the specimens. To eliminate the initial rigid-body motion due to manufacturing tolerances, a preload of 10 N was applied before the first scan. Following each loading step, the actuator position was kept constant for 15 min to allow polymer relaxation before acquiring the subsequent tomography scan. This procedure was repeated until the specimen failed, after which an additional scan captured the fracture surface. Fig. 3(c) presents a representative force-time curve illustrating the load-relaxation-scan sequence, highlighting the relaxation period at the 200 N step.

Tensile test specimens were machined using a 3-axis milling machine with water cooling to minimize thermal degradation of the polymer. The notch section featured a square cross-section of 1.5 × 1.5 mm^2 with a fillet radius of 1 mm, as shown in Fig. 1(c). The specimens were extracted from the center of injection-molded plaques, to investigate specimen of fiber orientation representative of functional components such as piston and packing rings. This location ensures alignment of the reinforcing fibers in the loading direction.

Reconstruction was carried out using a filtered back projection (FBP) algorithm implemented in MATLAB, provided by Helmholtz-Zentrum Hereon [47]. The resulting data sets had a voxel size of 1.28 µm. The volumetric data were subsequently downsampled from 32-bit float to 16-bit integer format to optimize processing. Gray value normalization was applied across all datasets using VGSTUDIO MAX 2024.1: air was assigned to 20 000, and a representative carbon fiber core to 35 000.

The effective spatial resolution, estimated to be approximately 3 µm, was limited by several factors, including sample drift, relaxation-induced motion blur, and precision of reconstruction. Sub-micrometer

features such as fine PTFE/MoS_2 boundaries and microcracks may therefore remain unresolved under these conditions.

Fracture behavior was assessed using digital volume correlation (DVC) applied to the SCT-scans. The analysis utilized the XDigital Volume Correlation module in Avizo 2024.1, using a global finite element-based DVC approach. The inherent microstructure pattern of the carbon fiber-reinforced PPS composite allowed accurate displacement tracking without the need for additional markers.

A global tetrahedral mesh with an average element size of 70 µm was used to evaluate strain distributions at the specimen level. To analyze the localized initiation and growth of fractures, selected Regions of Interest (ROI) of 400×400×400 $voxel^3$ were discretized using a structured tetrahedral mesh, refined to a final element size of 12 µm following a mesh convergence study. The selection of these ROIs was based on matching strain conditions, the absence of pre-existing damage, and the inclusion of the eventual fracture surface.

Systematic errors were evaluated by applying a virtual strain to the unloaded reference scans. The data sets were scaled by 2 % in the z-direction and correlated with their original counterparts. The recovered strain components confirmed accuracy, producing an average z-strain of 1.97 % and negligible x- and y-strain components, with a standard deviation of approximately 0.05 % in the z-direction.

To quantify strain localization, a strain concentration factor (SCF) was introduced based on the ratio between the local maximum von Mises equivalent strain ($\varepsilon_{eq,max}$) and the average von Mises equivalent strain of the ROI ($\varepsilon_{eq,mean}$)

$$SCF = \frac{\varepsilon_{eq,max}}{\varepsilon_{eq,mean}}. \quad (1)$$

The SCF served as a quantitative indicator of strain localization, highlighting critical regions such as fiber–matrix interfaces, porosity, and PTFE agglomerates. In particular, changes in SCF were observed before crack formation, suggesting that the evolution of SCF can be used as an early indicator of material failure.

For a selected ROI of approximately $400 \times 400 \times 400$ $voxel^3$ in size, an ISO150 threshold was defined between the ideal background (0) and the main material peak of the grayscale histogram for particle segmentation, while inclusions smaller than 9 voxel were ignored. The threshold was selected according to a procedure that was applied consistently to all datasets. This approach was necessary because the grayscale contrast between the PPS matrix and the PTFE/MoS_2 particles did not result in a clearly separated bimodal histogram, such that direct threshold identification from two distinct phases was not possible. Under these conditions, positioning the threshold between the background level and the main material peak provides a robust and reproducible segmentation criterion, as long as acquisition and reconstruction conditions are kept constant. To verify the plausibility of the selected threshold, the particle volume fraction determined from the segmented dataset was compared with the expected MoS_2 content calculated from the known weight fraction and the corresponding theoretical volume fraction of the composite. The satisfactory agreement between these values confirmed that the chosen threshold provides a realistic representation of the filler distribution and is therefore suitable for comparative evaluation.

Complementary microstructural analysis was performed using light optical microscopy (LOM) on mechanically polished surfaces extracted from the central region of the injection-molded plaques, ensuring alignment with the mechanically tested volume. Imaging was performed with a Zeiss Axio Imager.M2m microscope. The RGB images were post-processed using a custom workflow in Python 3.10.13 with the scikit-image, Matplotlib, and NumPy libraries [48]. The images were first converted to grayscale, followed by local contrast enhancement using adaptive histogram equalization (clip limit = 0.03) [49]. To evaluate PTFE/MoS_2 dispersion, four cross-sectional images were selected for statistical analysis. Segmentation was performed using a scaled Otsu thresholding algorithm, adjusted for local contrast variations [50]. Subsequent morphological filtering removed small artifacts and excluded features on the basis of eccentricity, allowing selective identification of the lubricant phase. These 2D results provided supporting information to the volumetric SCT datasets.

2.4. Thermomechanical testing

The thermomechanical behavior of the PPS matrix composites was characterized through dynamic mechanical analysis (DMA) and thermal expansion (TE) measurements. All experiments were carried out at the Transfercenter für Kunststofftechnik GmbH, Wels, Austria.

To gain insight into the matrix properties of the PPS composites, torsional DMA was conducted according to ISO 6721-7 [51], as this testing mode also provides insight into the shear loading experienced by the material under pressure forces from the piston and packing rings in the operating temperature range of reciprocating piston compressors. Rectangular specimens with dimensions of 3 mm in thickness, 10 mm in width, and 60 mm in length were prepared by precision cutting and surface grinding of injection-molded plaques. All samples were extracted along the axial direction, parallel to the melt flow, as indicated in Fig. 1(b). Measurements were conducted using a TA Instruments RSA-G2 system in a torsional test configuration. The storage modulus was recorded across a temperature range of 35 °C to 200 °C at a constant heating rate of 3 K/min. A free clamping length of 46 mm was used with a dynamic amplitude of 0.02 % applied at a frequency of 1 Hz. Modulus values were calculated as a function of temperature from the amplitude-time response.

To evaluate dimensional stability at elevated temperatures, a critical factor in maintaining minimal gap tolerances in piston ring applications, TE measurements were conducted. Specimens with nominal dimensions of $3 \times 10 \times 25$ mm^3 were extracted axially from the molded plaques by manual cutting and grinding. During preparation, continuous water cooling was applied to prevent thermal cycling of the polymer matrix. The thermal expansion testing followed the ISO 11359-2 standard [52] and was performed on a Netzsch TMA 402F1 thermomechanical analyzer. The testing sequence was carried out from 25 °C to 300 °C at a linear heating rate of 2 K/min, with helium introduced into the measurement chamber to prevent oxidative effects. Specimen elongation was recorded as a function of temperature, and the linear CTE was calculated on the basis of initial dimensions.

2.5. Standard testing

The mechanical behavior of PPS matrix composites was systematically characterized through tensile and compressive testing, conducted at the Institute of Materials Science and Technology, Technical University of Vienna, Austria. The test specimens were machined from the central region of the injection-molded plaques using an end mill, preserving the full thickness of the plaque. To evaluate the effect of fiber orientation on mechanical performance, samples were prepared in both the flow (axial) and transverse (lateral) directions relative to the molding direction, as illustrated in Fig. 1(b).

Tensile testing was performed using a Zwick Z050 universal testing machine on type 1BA samples, according to ISO527-2 [53]. A constant crosshead speed of 1 mm/s was applied. To assess the thermal sensitivity of the dry lubricated composites, specimens were heated to 23, 50, 80 and 110 °C for 2 h in a convection oven prior to and during the tensile testing. For each material variant, six specimens, three per orientation from separate plaques, were tested to ensure statistical robustness.

The compressive properties were evaluated following ISO 604 [54], using Type A specimens ($50 \times 10 \times 3$ mm^3) and Type B specimens ($10 \times 10 \times 3$ mm^3) to determine compressive modulus and compressive strength, respectively. The samples were sectioned from the molded plaques using a Mutronic Diadisc 4200 precision saw under continuous water cooling to minimize thermal damage. All compression tests were

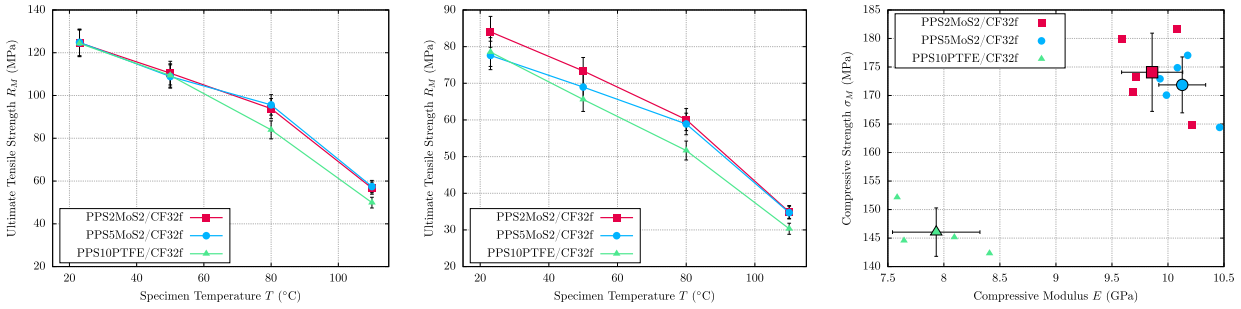

(a) Axial tensile test. (b) Lateral tensile test. (c) Compression test.

Fig. 4. Standard testing, tensile testing properties at different test specimen temperatures observed at a test speed of 1 mm/s with specimen oriented axially (a) and laterally (b) in relation to the injection molding direction. Compression testing results at a sample temperature of 23 °C and a test speed of 1 mm/s in (c).

carried out on a Zwick Roell Z020 universal test machine at a constant crosshead speed of 1 mm/min, with ambient temperature maintained at 23 °C. For each composite formulation, five specimens of each type were tested to ensure reproducibility and statistical significance.

3. Results

3.1. Standard testing

Tensile and compression tests were performed to evaluate the effect of the content of MoS_2 on the mechanical behavior of the PPS composites. The results are presented in Fig. 4. Given the strong influence of fiber orientation on the mechanical performance of short fiber reinforced polymers and its importance for the design of high-pressure hydrogen piston rings, tensile tests were performed in both axial and lateral directions relative to the injection molding direction as described in Fig. 1(b).

In all samples, a pronounced reduction in ultimate tensile strength is observed with increasing temperature. This reduction follows an approximately linear trend up to 80 °C, while above the glass transition temperature of PPS, a significant decline in mechanical properties is observed.

All three materials demonstrate comparable tensile strength at 23 °C and 50 °C in the axial direction, where the fiber alignment resulting from injection molding is most pronounced, reaching approximately 124 MPa and 110 MPa, respectively. At 80 °C, PPS10PTFE/CF32f shows a more pronounced decrease to 83 MPa, while PPS2MoS_2/CF32f and PPS5MoS_2/CF32f retain higher values around 93 MPa. However, at 110 °C the ultimate tensile strength of all materials converges to roughly 55 MPa, with statistical analysis suggesting that there are no significant differences between them.

In the lateral direction, a similar temperature-dependent trend is observed. At room temperature, materials with a higher dry lubricant content (PPS10PTFE/CF32f and PPS5MoS_2/CF32f) exhibit slightly lower tensile strength (approximately 78 MPa) compared to PPS2MoS_2/CF32f (84 MPa), although the results of one-way ANOVA suggest these differences are not statistically significant. As the specimen temperature is increased to 50 °C, the tensile strength decreases by approximately 15 % to an average of 69 MPa. At 80 °C, MoS_2-containing compounds outperform PPS10PTFE/CF32f, achieving 60 MPa versus 50 MPa. At the final test specimen temperature of 110 °C the compounds exhibit a tensile strength of 30 MPa to 35 MPa

In general, the samples tested in the axial direction consistently exhibited superior tensile strength at all temperatures, with room temperature values approximately 30 % higher than those obtained from the laterally oriented test specimens.

The results of the compressive test reveal distinct differences in the mechanical performance of PPS compounds depending on the type of dry lubricant used. PPS10PTFE/CF32f, which contains PTFE, exhibits a significantly lower compressive strength, reaching only 146 MPa, compared to the MoS_2-lubricated compounds, which achieve values in the range of 171 MPa to 174 MPa. This corresponds to an approximate 15 % reduction in ultimate compressive strength for the PTFE-lubricated material. Among the compounds containing MoS_2, no statistically significant differences in compressive strength were observed between PPS2MoS_2/CF32f and PPS5MoS_2/CF32f, as indicated by the Welch's t-test ($p = 0.575$).

A similar trend is observed in the compressive modulus. The highest modulus is recorded for PPS5MoS_2/CF32f at 10.1 GPa, followed closely by PPS2MoS_2/CF32f at 9.8 GPa. Although these values strongly suggest superior stiffness for the MoS_2-based compounds, the variability within the data set precludes a definitive ranking in the range of 2 wt.% to 5 wt.% MoS_2. PPS10PTFE/CF32f shows a significantly lower compressive modulus of 8.3 GPa, representing a reduction of approximately 17 % relative to the MoS_2 lubricated materials. A detailed summary of the mechanical properties is provided in Table 3.

3.2. Thermomechanical properties

The DMA results are presented in Fig. 5(a), which shows the temperature-dependent storage modulus (G') for the three polymer compositions investigated. In the operational temperature range of 35 °C to 85 °C, all three materials exhibit an approximately linear decline in storage modulus. PPS5MoS_2/CF32f, the reference compound containing PTFE, starts with a lower initial storage modulus of 3.7 GPa, while both MoS_2-filled formulations (PPS10PTFE/CF32f and PPS2MoS_2/CF32f) exhibit slightly higher initial values of 3.8 GPa. However, due to measurement variability, the difference between PPS10PTFE/CF32f and PPS2MoS_2/CF32f is within the standard deviation and therefore not statistically significant, as detailed in Table 4. The onset of the glass transition region is consistent across all compositions and starts at approximately 90 °C, confirming that the transition is primarily governed by the PPS matrix and is not affected by the presence of MoS_2 or PTFE [55]. At elevated temperatures, all samples converge to the rubber-elastic plateau, with storage modulus values of approximately 1.2 GPa at 125 °C, indicating similar high-temperature mechanical behavior regardless of the lubricant additive used.

Thermomechanical analysis (TMA) was performed using dilatometry to continuously monitor the dimensional changes of each PPS-based composite in the temperature range of 25 °C to 200 °C. Fig. 5(b) shows representative first heating cycles for all sample compounds. Consistent with the trends observed in DMA testing, the compound containing PTFE exhibits a more pronounced dimensional increase within the 30 °C to 90 °C interval compared to the MoS_2 lubricated counterparts (PPS10PTFE/CF32f and PPS2MoS_2/CF32f). PPS is known to undergo a slight contraction near its glass transition temperature, a phenomenon attributed to a combination of cold crystallization, moisture release, and relaxation effects of polymer chains [56]. This contraction is

Table 3
Tensile and compressive properties at a temperature of 23 °C.

Abbreviated form	Tensile strength axial (MPa)	Tensile strength lateral (MPa)	Ultimate compressive strength (MPa)	Compressive modulus (GPa)
PPS10PTFE/CF32f	124 ± 6	78 ± 4	146 ± 4	7.9 ± 0.3
PPS2MoS$_2$/CF32f	124 ± 5	84 ± 4	174 ± 7	9.8 ± 0.3
PPS5MoS$_2$/CF32f	124 ± 6	77 ± 4	171 ± 5	10.1 ± 0.2

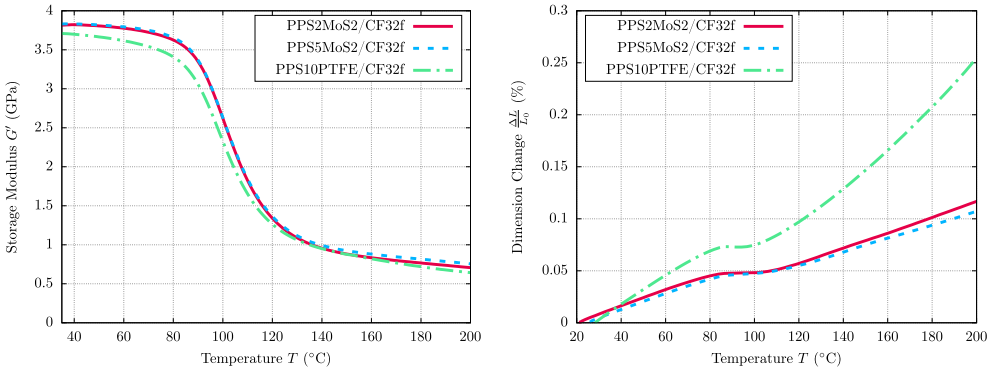

(a) DMA (b) TMA

Fig. 5. Thermomechanical testing, results of DMA testing conducted at a controlled heating rate of 3 K/min in a range of 35 °C to 200 °C (a), TMA results for the first heating cycle from 25 °C to 300 °C at a heating rate of 2 K/min (b).

Table 4
Thermomechanical properties summarizing the storage Modulus at room temperature from DMA testing data and calculated linear CTE from TMA testing at a piston ring operating temperature range of 30 °C to 90 °C.

Abbreviated form	Storage modulus (MPa)	CTE (ppm/K)
PPS10PTFE/CF32f	3538 ± 162	7.0 ± 0.3
PPS2MoS$_2$/CF32f	3726 ± 14	8.0 ± 1.3
PPS5MoS$_2$/CF32f	3542 ± 196	10.2 ± 1.6

evident in all samples, but is most pronounced in PPS5MoS$_2$/CF32f, which demonstrates a noticeably sharper inflection in the expansion curve than PPS10PTFE/CF32f and PPS2MoS$_2$/CF32f. Below the glass transition region, all composites exhibit nearly linear thermal expansion behavior. Above 100 °C, the expansion of PPS10PTFE/CF32f and PPS2MoS$_2$/CF32f remains linear, while the PTFE-containing sample shows a progressive increase in its expansion rate.

Given the relevance of thermal expansion for applications such as reciprocating compressor pistons and packing rings, Table 4 summarizes the calculated CTE in the typical operating range of 30 °C to 90 °C. In this regime, PPS5MoS$_2$/CF32f displays the highest linear CTE at 10.2 ± 1.6 ppm/K, while PPS10PTFE/CF32f and PPS2MoS$_2$/CF32f exhibit comparable values of 7.0 ± 0.3 ppm/K and 8.0 ± 1.3 ppm/K, respectively.

3.3. Tribometry

The tribological evaluation of short-fiber-reinforced PPS composites provides fundamental insight into friction and wear behavior as a function of the type and concentration of solid lubricant additives. The results of the tribological tests are summarized in Fig. 6. For PPS10PTFE/CF32f and PPS5MoS$_2$/CF32f, the CoF plots exhibit a distinct run-in phase, characterized by an initially high and fluctuating CoF that abruptly decreases to lower values after approximately 800 cycles and 2500 cycles, respectively.

For the PTFE lubricated compound, PPS10PTFE/CF32f, the friction curve exhibits a transitional tribological regime after run-in, with a slight increase in friction between approximately 800 cycles and 10 000 cycles. Finally, a stable CoF of approximately 0.2 can be observed for the remainder of the test. This progression indicates surface adaptation and tribofilm formation during the initial sliding phase, which eventually leads to steady-state friction conditions, as previously reported [24,25]. The duration and magnitude of the run-in phase varies slightly between individual test runs.

During the run-in PPS5MoS$_2$/CF32f exhibits a 40 % higher CoF than PPS10PTFE/CF32f and exhibited a longer run-in period, but subsequently the CoF drops to values below 0.1 toward the end of the test. The steady-state condition demonstrates high repeatability, as evidenced by the low standard deviation.

In contrast, PPS2MoS$_2$/CF32f does not exhibit distinct run-in behavior, and its CoF remains at the initial high level above 0.3 throughout the duration of the test. The absence of a low-friction steady state in PPS2MoS$_2$/CF32f is attributed to its lower MoS$_2$ content.

PPS10PTFE/CF32f and PPS5MoS$_2$/CF32f both show a high initial wear rate (Figs. 6(b) and 6(f)) with significant differences in total run-in wear between the individual test results, likely attributed to manufacturing imperfections, geometric inconsistencies of the test pins, and the deposition of a polymer tribo-film on the steel counter surface.

The onset of the steady-state CoF regime for PPS10PTFE/CF32f and PPS5MoS$_2$/CF32f is observed approximately at 800 and 2500 cycles, respectively, coinciding with the establishment of a constant low wear rate. Fig. 7, which presents the average wear curves of PPS10PTFE/CF32f and PPS5MoS$_2$/CF32f after the run-in phase, illustrates their wear behavior within the steady-state operating regime.

In contrast, PPS2MoS$_2$/CF32f exhibits a pronounced linear wear trend throughout the test, leading to complete depletion of the test pin and aborting the test runs at approximately 4000 cycles. For PPS10PTFE/CF32f and PPS5MoS$_2$/CF32f, the specific wear rates were determined by linear regression of the wear data within a 10 000 cycles to 20 000 cycles interval, while PPS2MoS$_2$/CF32f was evaluated in a range of 0 cycles to 4000 cycles. The resulting wear rates, together with the corresponding CoF values, are summarized in Table 5 showing that PPS10PTFE/CF32f and PPS5MoS$_2$/CF32f exhibit stable and comparatively low specific wear rates in the steady-state regime, ranging from 13×10^{-8} mm^3/(N m) to 23×10^{-8} mm^3/(N m), while PPS2MoS$_2$/CF32f shows a markedly higher value of 9049×10^{-8} mm^3/(N m).

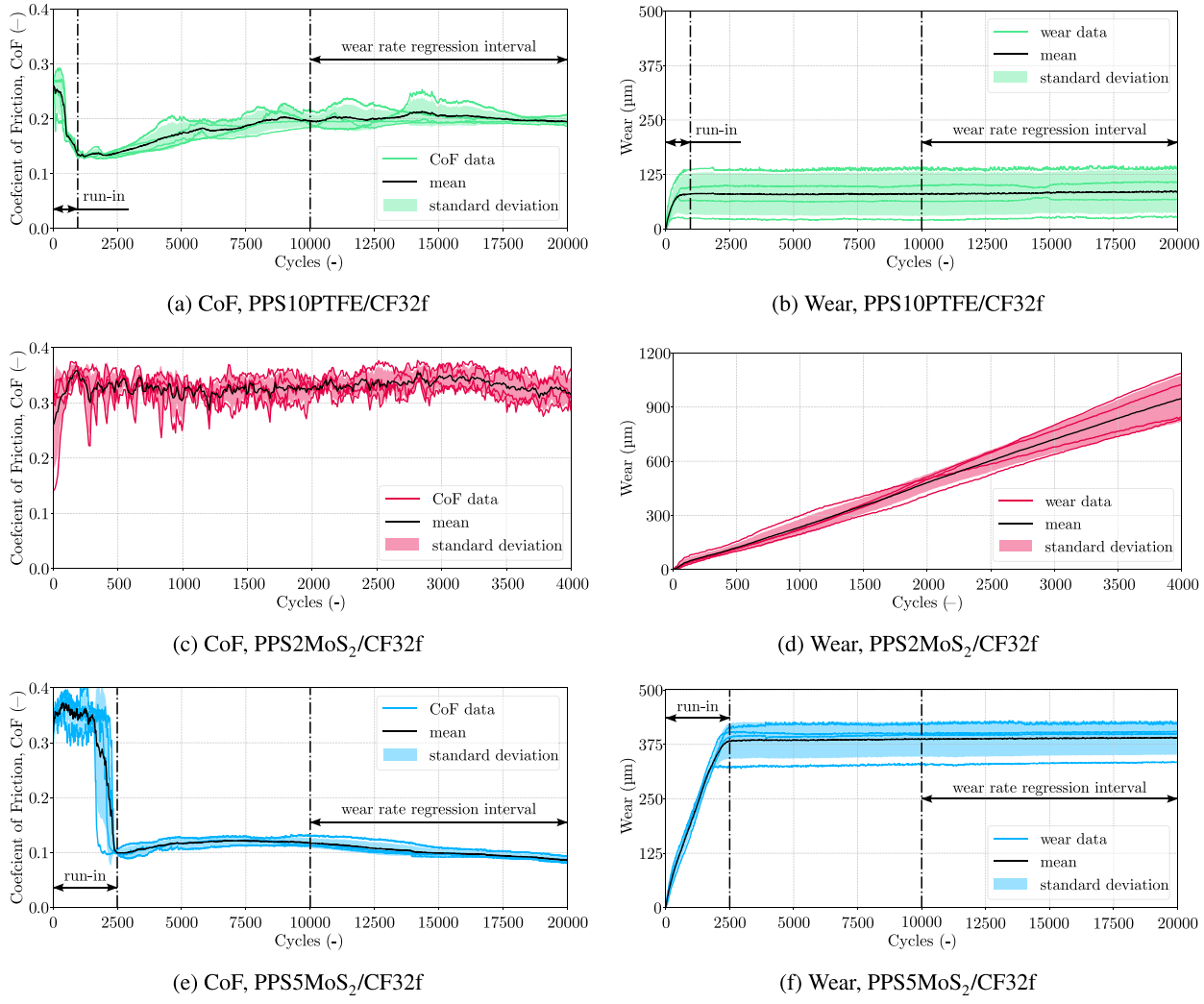

(a) CoF, PPS10PTFE/CF32f

(b) Wear, PPS10PTFE/CF32f

(c) CoF, PPS2MoS$_2$/CF32f

(d) Wear, PPS2MoS$_2$/CF32f

(e) CoF, PPS5MoS$_2$/CF32f

(f) Wear, PPS5MoS$_2$/CF32f

Fig. 6. Tribology, measured CoF and wear, showing individual test runs (colored lines), arithmetic mean (black lines) and standard deviation (shaded colored regions) for PPS10PTFE/CF32f (a), (b), PPS2MoS$_2$/CF32f (c), (d) and PPS5MoS$_2$/CF32f (e), (f).

Table 5
Summary of tribological testing results, including the mean value and standard deviation for each, coefficient of friction and specific wear rate (steady-state regime).

Abbreviated form	Run-in duration (cycles)	Run-in wear (µm)	Coefficient of friction (–)	Specific wear rate ($mm^3/N/m\,10^{-8}$)
PPS10PTFE/CF32f	800	80.5 ± 40.4	0.20 ± 0.015	22.6 ± 9.6
PPS2MoS$_2$/CF32f	NA	NA	0.33 ± 0.025	9049 ± 1338
PPS5MoS$_2$/CF32f	2500	382.8 ± 35.6	0.09 ± 0.004	12.8 ± 8.3

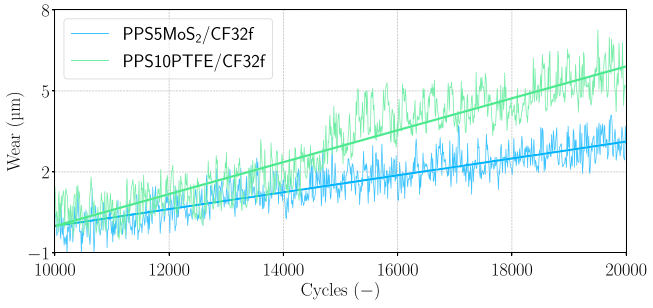

Fig. 7. Tribology, total measured average wear of PPS10PTFE/CF32f and PPS5MoS$_2$/CF32f following the run-in phase, illustrating the steady-state tribological behavior of the PPS matrix composites. Calculated linear regression lines are overlaid for comparison.

3.4. Fracture behavior and micro-mechanics

LOM micrography of short-fiber-reinforced PPS matrix composites, presented in Fig. 8, reveal distinct microstructural features for each composition. The images were acquired from the central region of the sample plates, with the imaging plane aligned with the injection molding direction, as illustrated in Fig. 1(b). These micrographs serve as reference images for the subsequent in-situ SCT tensile testing.

Across all three composites, the fibers exhibit a similar orientation pattern, with carbon fibers predominantly aligned along the injection molding direction. No evidence of large-scale porosity or significant defects is observed at the fiber–matrix interface. In addition to the light-gray fibers embedded within the darker-shaded PPS matrix, dark spherical PTFE particles PPS10PTFE/CF32f, varying in size, are distributed throughout the matrix, where some of these PTFE particles are located directly at the fiber–matrix interface. In PPS2MoS$_2$/CF32f

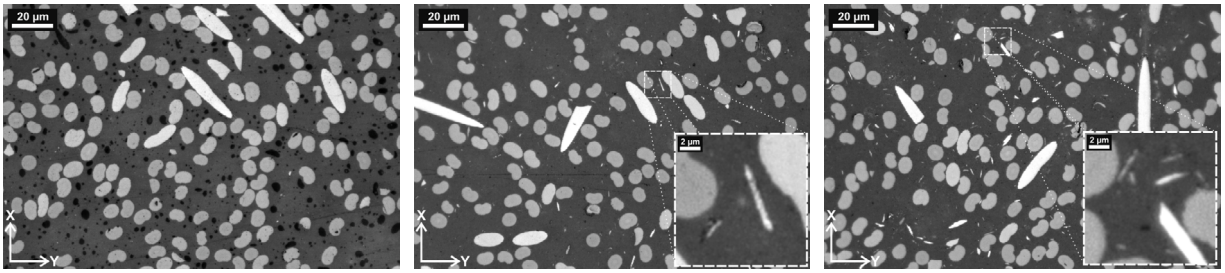

(a) PPS10PTFE/CF32f (b) PPS2MoS_2/CF32f (c) PPS5MoS_2/CF32f

Fig. 8. LOM, microstructure of PPS test specimens perpendicular to injection molding direction. Carbon fibers (bright) are embedded in the PPS matrix (gray) and dark PTFE particles in (a), as well as small light-gray needle-shaped MoS_2 particles shown in (b) and (c).

Table 6
Lubricant particle metrics (fraction, diameter and aspect ratio) from digital shape analysis of LOM images.

Abbreviated form	Lubricant volume fraction (vol.%)	Average sectional diameter (µm)	Sectional aspect ratio (−)
PPS10PTFE/CF32f	6.68 ± 0.39	2.03 ± 0.06	1.63 ± 0.07
PPS2MoS_2/CF32f	0.61 ± 0.03	1.71 ± 0.29	2.03 ± 0.23
PPS5MoS_2/CF32f	1.61 ± 0.01	1.85 ± 0.07	2.21 ± 0.14

and PPS5MoS_2/CF32f (Figs. 8(b) and 8(c), respectively), bright needle-shaped MoS_2 particles, of sizes ranging from 1 µm to 3 µm, are uniformly distributed within the PPS matrix. Although particle size and shape remain consistent, the higher MoS_2 content in PPS5MoS_2/CF32f results in a noticeably higher particle density compared to PPS2MoS_2/CF32f.

Digital shape analysis of the LOM micrographs further confirms the qualitative observations, revealing clear distinctions in particle morphology among the different solid lubricant particles. The majority of the MoS_2 particles show an elongated rodlike form, characterized by a relatively high average aspect ratio ranging from 2.03 to 2.21. No statistically significant variation of the aspect ratio is detected between the MoS_2 particles in PPS2MoS_2/CF32f and PPS5MoS_2/CF32f, suggesting that the morphology of these particles is comparable. In contrast, the PTFE particles appear noticeably more rounded in the LOM images, exhibiting a lower average aspect ratio of 1.63, consistent with their visually more spherical geometry.

Analysis of the mean particle size indicates that the MoS_2 particles in PPS2MoS_2/CF32f and PPS5MoS_2/CF32f possess comparable dimensions, with average sizes between 1.71 µm to 1.85 µm, which implies that changes in the lubricant content do not significantly affect the particle size or distribution within the PPS matrix. In comparison, PPS10PTFE/CF32f, with PTFE as the solid lubricant, shows a slightly larger characteristic particle size of approximately 2.03 µm.

The optical contrast between the lubricant phases and the surrounding PPS matrix allowed for precise segmentation and quantification of the lubricant volume fractions. The measured values are in excellent agreement with the theoretical volume fractions calculated from the known mass fractions and the material densities listed in Table 2. A comprehensive summary of the image analysis results, including particle morphology and size parameters, is provided in Table 6.

Fig. 9 shows a representative slice of the SCT tomographic volume in which the PTFE and MoS_2 particles have been digitally segmented. For clarity, the segmented lubricating particles are colored yellow. The SCT images confirm the observations from the LOM analysis. No evidence of MoS_2 agglomeration is found in PPS2MoS_2/CF32f or PPS5MoS_2/CF32f, indicating that the lubricant is homogeneously distributed within the PPS matrix. In PPS10PTFE/CF32f the higher volume fraction of PTFE is apparent. Although no agglomeration of large scale PTFE particles is observed, a higher number of particles is located at the fiber–matrix interface.

The workflow for determining crack initiation mechanisms, illustrated in Fig. 10, is based on a stepwise evaluation of DVC analyzes performed on SCF data obtained from in situ SCT during tensile testing on PPS10PTFE/CF32f and PPS5MoS_2/CF32f. These materials were selected based on the results of previous tribological tests, while PPS2MoS_2/CF32f was excluded from further analysis due to insufficient tribological performance. The tensile specimens were machined such that the loading direction was parallel to the injection molding direction, which corresponds to the predominant fiber alignment in load direction. It was observed that injection molding of short-fiber reinforced polymers can introduce orientation gradients across the specimen thickness, typically characterized by a skin-core structure with locally varying fiber alignment which has been investigated in previous studies [24]. To minimize the influence of such gradients on the strain localization analysis, the in-situ SCT tensile test investigations were performed in the central region of the specimen, away from the outer skin layers. The analyzed volumes therefore represent the characteristic fiber orientation resulting from the manufacturing process and are considered representative for piston and packing ring components produced under comparable processing conditions. At each incremental load step, the SCF is recorded for the whole SCT volume and statistically analyzed to track the evolution of local strain states within the composite. The regions exhibiting large changes in the standard deviation of the SCF are subsequently isolated from the DVC datasets, highlighting zones of pronounced localized redistribution of strain. These zones are then examined in relation to their spatial positions and adjacent microstructural features, allowing correlation with specific damage initiation modes such as void nucleation or interfacial cracking. This workflow facilitates the identification of dominant crack initiation mechanisms, providing critical insight into the fundamental processes governing composite failure.

In PPS10PTFE/CF32f, the injection molding process combined with the mismatch in thermal expansion coefficients between the PPS matrix and the carbon fibers leads to the inherent formation of defects at the phase boundaries. These defects are most frequently observed at the fiber ends, where the lower thermal expansion of carbon fibers compared to the surrounding PPS matrix promotes the initiation of local voids (Fig. 11(a)). A representative tomographic cross-section at an axial force of 10 N, where the load is applied vertically in the image, confirms this behavior, with voids visible in blue. Figs. 11(b) and 11(c) show tomographic cross-sections overlaid with SCF obtained from DVC analysis. The yellow-red surfaces represent the upper 60 % of the local strain values, highlighting the regions with maximum strain accumulation. These specific load steps were selected because the SCF analysis indicated the onset of significant void opening at 170 N, while 200 N represents the final load step prior to the fracture of the specimen.

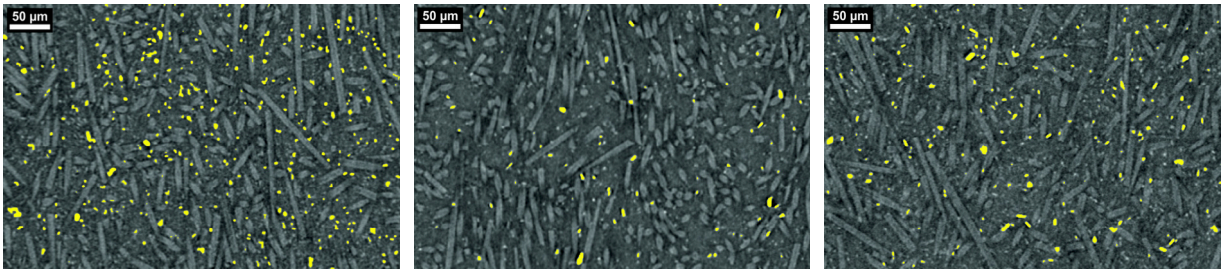

(a) PPS10PTFE/CF32f (b) PPS2MoS$_2$/CF32f (c) PPS5MoS$_2$/CF32f

Fig. 9. SCT, cross-sections of the unloaded samples with segmented (yellow) PTFE particles in (a), and MoS$_2$ in (b) and (c).

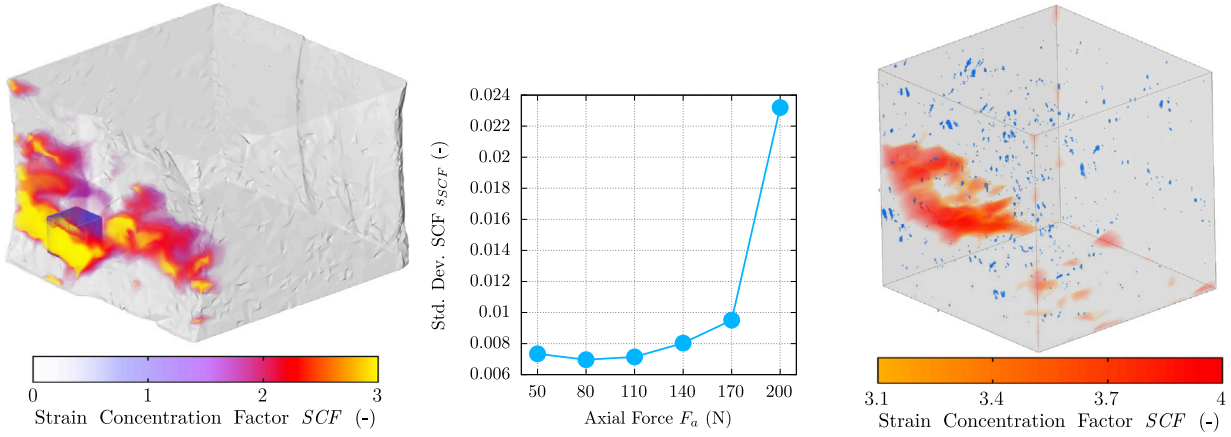

(a) DVC and ROI identification (b) Strain concentration factor (c) Analysis of damage initiation

Fig. 10. DVC, workflow to localize the crack initiation in fiber reinforced PPS matrix composites demonstrated on the example of PPS2MoS$_2$/CF32f. Sub-figure (a) demonstrates the identification of high SCF regions by conducting a DVC analysis on the complete SCT scan volume and subsequent ROI selection at an axial load of 170 N, (b) the analysis of SCF in the ROI volume for each load step and (c) the overlay of defects and high SCF value voxels to analyze damage initiation under load.

Comparison of the segmentation of the defects and the voids at preload and under an axial force of 170 N reveals that the dominant mechanism in PPS10PTFE/CF32f is the growth of preexisting porosities, manifested primarily as penny-shaped interface cracks [57]. Only a few new isolated defects are observed, typically at the fiber ends and PTFE-fiber phase boundaries. When the axial force increases to 200 N, additional void opening becomes evident, accompanied by an abrupt crack propagation, particularly along the interfaces of PTFE particles dispersed within the matrix. These findings indicate that during the early stages of loading, the response of the material is governed mainly by the evolution of the inherent microstructural features rather than by the nucleation of entirely new cracks or defects.

A comparison of DVC strain fields with digital segmentation of porosities in the unloaded state (Fig. 11(b)) further supports this interpretation. Regions of high SCF generally coincide with fewer initial imperfections, suggesting that porosity is not uniformly distributed with respect to load-bearing capacity. Increasing the axial load to 170 N does not produce a significant number of new voids in these regions of high SCF. However, at 200 N (shown in Fig. 11(c)), the initiation and growth of the cracks are clearly observable throughout the PPS matrix. PTFE particles act as weak points in the matrix and promote crack bridging, thereby influencing fracture paths. This is accompanied by a redistribution of strain. Local regions of initially high strain undergo a reduction in concentration, while the remaining load-bearing sections experience increased strain, highlighting the progressive transfer of stress as damage develops.

Analysis of porosity and crack segmentation in PPS5MoS$_2$/CF32f reveals distinct damage evolution and deformation behavior compared to PPS10PTFE/CF32f. Representative tomography slices with an increasing axial load are presented in Fig. 12.

At the initial 10 N preload (Fig. 12(a)), only a few defects are detected, located primarily at the MoS$_2$-PPS interface boundaries (segmented in blue). When the axial load increases to 170 N as shown in Fig. 12(b), these small-scale pores increase in size, while additional pores are created. Furthermore, localized larger scale defects appear at the fiber–matrix interface, particularly in regions of high strain (shown in red) and where fibers are oriented orthogonally to the loading direction.

During the final load step prior to fracture (200 N), preexisting cracks exhibit pronounced growth, together with the formation of new voids, as well as crack bridging through the PPS matrix. Although MoS$_2$ particles do not significantly influence crack growth, they remain the main sites for defect creation.

The SCT cross-sections overlaid with DVC fields (Figs. 12(b) and 12(c)) highlight a single region of maximum strain concentration originating from the free surface of the tensile specimen at 170 N, which intensifies and expands at 200 N. Up to 170 N, new cracks and porosities form mainly at MoS$_2$ particles and through localized debonding at fiber–matrix interfaces. At 200 N, these features grow further, with porosities and interface debonding concentrated in regions that coincide with high strain concentrations and inclusions of MoS$_2$.

Although PPS10PTFE/CF32f and PPS5MoS$_2$/CF32f exhibit similar ultimate tensile strengths, their damage mechanisms differ markedly. In PPS5MoS$_2$/CF32f, crack formation is dominated by fiber–matrix interface failure, with cracks propagating along fiber directions. In contrast, PPS10PTFE/CF32f exhibits crack bridging facilitated by PTFE

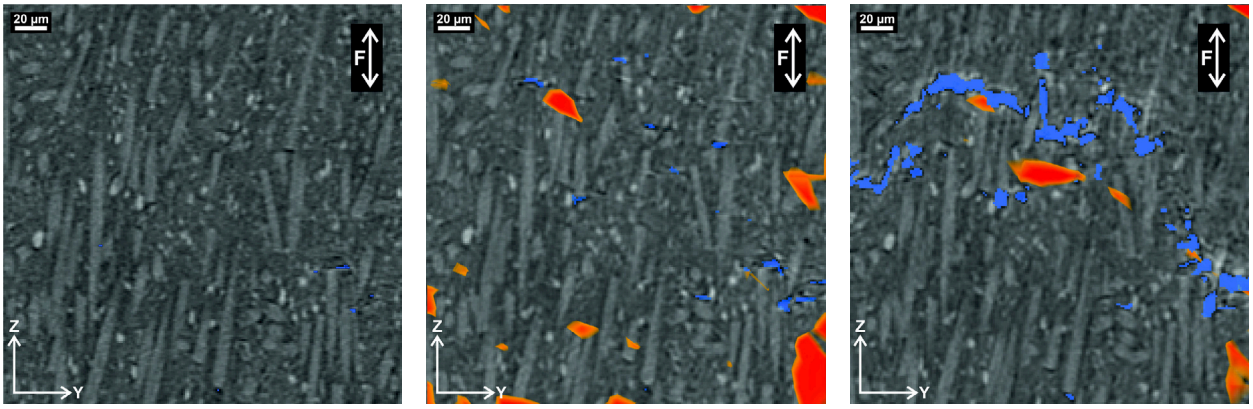

(a) Porosities at 10 N (b) SCF and porosities at 170 N (c) SCF and porosities at 200 N

Fig. 11. DVC, crack growth in PPS10PTFE/CF32f, illustrated by representative SCT cross-sectional images in the crack initiation region. Digitally segmented defects/porosities (blue) are shown at the initial load of 10 N, 170 N, and 200 N in (a), (b), and (c), respectively. The yellow-red surfaces represent the upper 60 % of the local SCF overlaid at axial forces of 170 N in (b) and 200 N in (c).

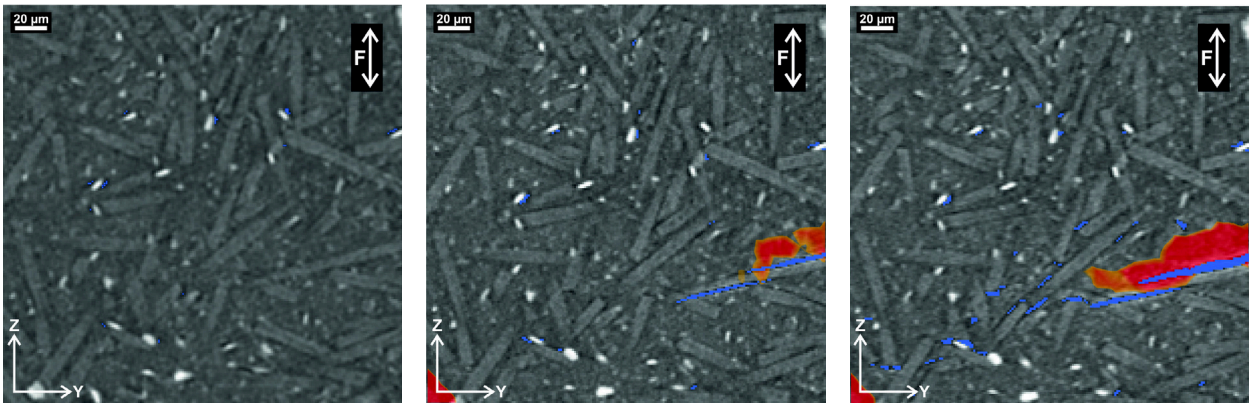

(a) Porosities at 10 N (b) SCF and porosities at 170 N (c) SCF and porosities at 200 N

Fig. 12. DVC, crack growth in PPS5MoS$_2$/CF32f, illustrated by representative SCT cross-sectional images in the crack initiation region. Digitally segmented defects/porosities (blue) are shown at the initial load of 10 N, 170 N, and 200 N in (a), (b), and (c), respectively. The yellow-red surfaces represent the upper 60 % of the local SCF overlaid at axial forces of 170 N in (b) and 200 N in (c).

particles, which alters the crack path and contributes to differences in fracture behavior.

The previous observation can be confirmed by an additional analysis of the defect formation mechanisms by examining the void distribution in the DVC-ROIs as presented in Figs. 13 and 14.

Fig. 13 provides detailed insight into the formation of defects in PPS10PTFE/CF32f highlighting voids in the ROI in orange. The image shows the 3D segmentation of the voids at increasing load, starting with the initial preload of 10 N where small defects (<7 µm) are distributed throughout the region of interest. At an increased load of 170 N the existing porosities in the ROI have increased in size, while few additional defects have formed. During the final load step before fracture, reaching 200 N, a sudden increase in void volume can be observed. The initial formation of the fracture surface can be observed, where the topology of the crack volume appears rough and irregular throughout the complete ROI volume. This confirms the observations of the 2D segmentations, where crack growth in PPS10PTFE/CF32f is governed by the presence of PTFE particles.

The behavior of PPS5MoS$_2$/CF32f observed in the 2D tomography slices shown in Fig. 12 can be confirmed in the 3D segmentation illustrated in Fig. 14. PPS5MoS$_2$/CF32f initially also shows a homogeneous distribution of micron-scale material defects and porosities throughout the region of interest, again highlighted as orange volumes. Increasing the axial load in PPS5MoS$_2$/CF32f leads to isolated debonding of the fiber matrix interface at fibers predominantly oriented in the xy-plane at 170 N. An increase in the load to 200 N exhibits the formation of a fracture plane in which the crack bridging through the PPS matrix, connecting isolated void patches and expanding the crack from the free surface to the bulk volume of the tensile test specimen.

Further evaluation of failure behavior in short-fiber reinforced PPS composites was conducted on tomographic scans of tensile test fracture surfaces. The high-resolution reconstructions shown in Figs. 15(b) and 15(c) allow the identification and characterization of different fracture mechanisms illustrated in Fig. 15(a), revealing differences in failure modes for the different types of lubricants presented in this study. In both PPS10PTFE/CF32f and PPS5MoS$_2$/CF32f specimens, fiber pullout, matrix cracking, and fiber–matrix debonding are consistently observed as the dominant mechanisms. However, their prevalence and interaction vary substantially depending on the lubricant incorporated into the matrix.

In PPS10PTFE/CF32f, shown in Fig. 15(b), the fracture process is dominated by fiber–matrix debonding. The propagation of cracks is strongly influenced by the presence of PTFE particles embedded within the PPS matrix. The resulting fracture surfaces exhibit a rough and irregular topology, where PTFE acts as crack-bridging sites, limiting the effective strength of the matrix and confirming the observations obtained from the DVC analysis. The areas surrounding the failed fiber–matrix interfaces show additional roughness, indicating partial

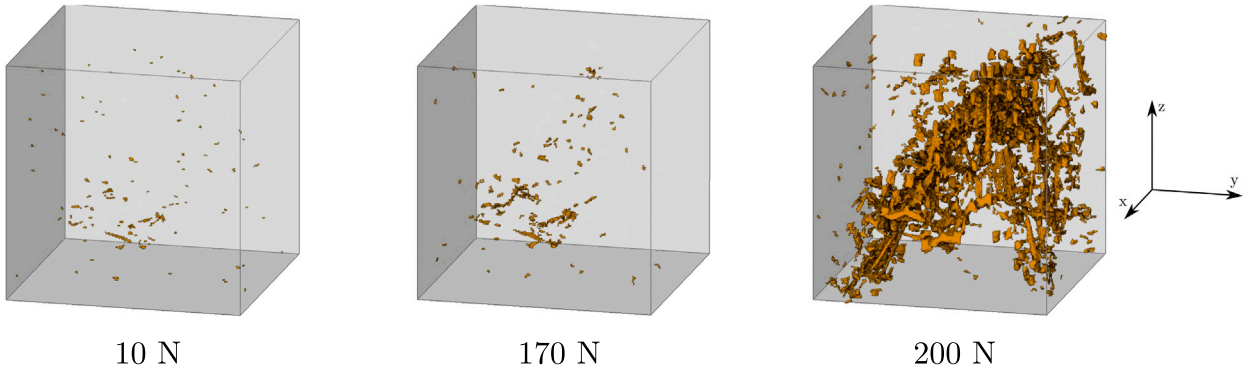

Fig. 13. DVC, crack propagation process in PPS10PTFE/CF32f showing digital segmentation of the porosities (orange surface) at 10, 170 and 210 N load step in the $400 \times 400 \times 400$ voxel^3 large ROI.

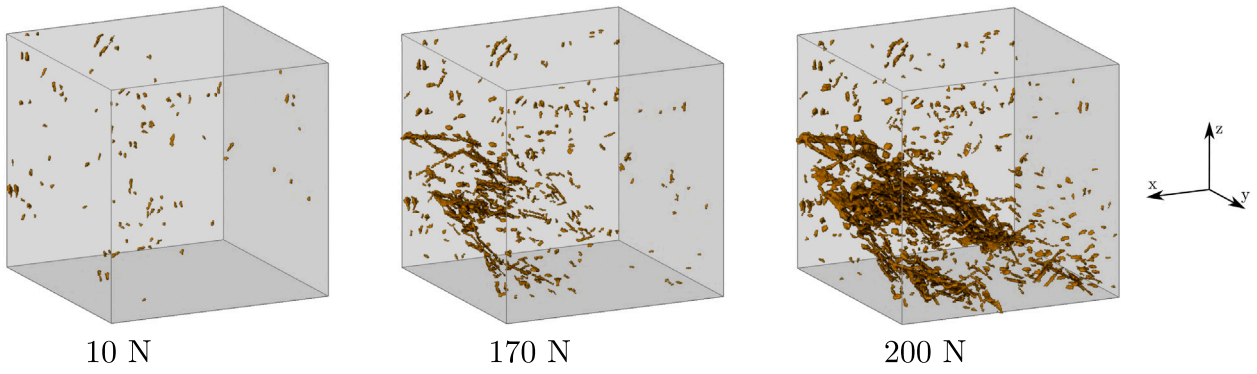

Fig. 14. DVC, crack propagation process in PPS5MoS$_2$/CF32f showing digital segmentation of the porosities (orange surface) at 10, 170 and 210 N load step in the $400 \times 400 \times 400$ voxel^3 large ROI.

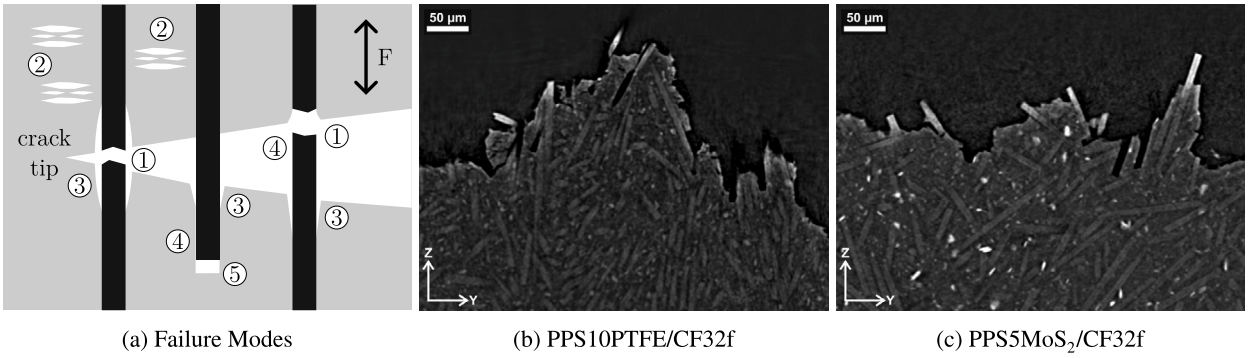

Fig. 15. SCT, synchrotron tomography cross-sections of the fracture surfaces of PPS test specimens after tensile testing. (a) Schematic illustration of typical failure modes in short fiber–reinforced polymers: (1) fiber fracture, (2) matrix cracking, (3) delamination, (4) fiber pullout, and (5) fiber end cracking. (b)–(c) Representative SCT cross-sections PPS specimens fracture surfaces. Brighter rod-shaped carbon fibers are embedded in the PPS matrix (gray), and brighter PTFE particles in (b) and white MoS_2 particles in (c) are visible.

adhesion of the polymer matrix to the fiber surfaces at the point of failure. Larger PTFE inclusions also promote the initiation of microcracks at fiber–matrix interfaces and contribute to crack bifurcation, thus accelerating fiber detachment and premature failure under tensile loading. Furthermore, PTFE particles serve as local stress concentrators, triggering secondary cracking within the surrounding matrix. Collectively, these effects produce a more irregular and heterogeneous fracture topology in PPS10PTFE/CF32f.

By contrast, the PPS5MoS$_2$/CF32f specimen containing 5 wt.% MoS_2 exhibited a markedly different fracture response. A representative tomographic cross-section shown in Fig. 15(c) reveals a greater prevalence of fiber pullout, with fibers cleanly extracted from the matrix. Compared to the PTFE-modified composite, the fracture surface appears noticeably smoother. Interestingly, fiber orientation plays a reduced role in governing crack propagation in PPS5MoS$_2$/CF32f. In regions where the fibers align with the loading direction, the cracks propagate

preferentially along the fiber–matrix interfaces, leading to a clean fiber pullout. Fibers oriented orthogonally to the applied load also fail predominantly at the interface, with matrix cracking perpendicular to the tensile axis through the surrounding matrix. This shift in fracture behavior underscores the distinct role of MoS_2 in altering interfacial adhesion and modifying the overall crack path.

4. Discussion and conclusions

This work presents a systematic investigation of the influence of MoS_2 on the thermo-mechanical, microstructural, and tribological behavior of PPS composites reinforced with short-carbon-fibers, compared to a reference material lubricated with PTFE. The study focuses on assessing their suitability for application in high-pressure hydrogen compressors. A comprehensive experimental approach combined standard thermo-mechanical and tribological testing with advanced SCT imaging and DVC analyzes to provide information on the mechanisms that govern the performance of MoS_2-lubricated PPS composites. The findings reveal pronounced trade-offs between mechanical strength, dimensional stability, and wear resistance as a function of dry-lubricant type and content, highlighting the need for an optimization of composite formulation.

During mechanical tests, MoS_2-lubricated compounds exhibit superior compressive load performance compared to PPS10PTFE/CF32f. In tensile tests, both PPS2MoS_2/CF32f and PPS5MoS_2/CF32f demonstrate better strength retention at elevated temperatures. This is attributed to a stronger fiber–matrix bonding, because PPS adheres better to MoS_2 than to PTFE. The presence of large PTFE particles at the fiber–matrix interface reduces the interface bonding strength and impedes stress transfer from the PPS matrix to the carbon fiber reinforcement. These effects have been documented in previous studies that reported the detrimental influence of PTFE phase separation on the mechanical integrity of composite systems [24,25]. In contrast, both PPS2MoS_2/CF32f and PPS5MoS_2/CF32f exhibit a homogeneous dispersion of the MoS_2 lubricant within the matrix, with no evidence of particle agglomeration at the fiber–matrix interfaces. Variations of MoS_2 up to a content of 5 wt.% do not produce a statistically significant difference in overall mechanical performance. The thermo-mechanical behavior of the composites is strongly influenced by the choice of solid lubricant phase. The MoS_2-filled materials (PPS2MoS_2/CF32f and PPS5MoS_2/CF32f) demonstrate superior thermo-mechanical stability, exhibiting higher storage moduli in the operating temperature range. This behavior indicates improved mechanical performance under the elevated temperature conditions typically encountered in hydrogen compressor piston ring applications. Although the glass transition temperature remains consistent in all formulations, the DMA results underscore the importance of effective cooling of PPS based piston and packing rings during operation to maintain performance stability. Furthermore, the MoS_2-containing composites (PPS2MoS_2/CF32f and PPS5MoS_2/CF32f) exhibit not only the lowest CTE but also a more linear thermal expansion response. This combination suggests improved dimensional stability at elevated temperatures, which is an essential attribute to minimize clearance gaps, reduce blow-by, and ensure consistent sealing performance in high-temperature, high-pressure compressor environments.

Tribological tests under hydrogen atmosphere clearly demonstrate the beneficial effects of MoS_2 as a solid lubricant, highlighting its ability to significantly reduce friction and wear even at moderate concentrations of 5 wt.% (1.6 vol.%). PPS5MoS_2/CF32f exhibits particularly low and stable coefficients of friction during steady-state operation, suggesting the formation of a continuous and effective transfer film at the sliding interface. Previous investigations reporting the initiation of a PTFE-based tribofilm were also confirmed under hydrogen atmospheres for the reference material PPS10PTFE/CF32f [25]. However, the present results indicate that MoS_2 contents greater than 0.6 vol.% are necessary to ensure satisfactory tribological performance, as the material does not develop a stable transfer layer and consequently exhibits elevated coefficients of friction. The test setup was designed to closely replicate realistic service conditions for PPS-based piston and packing seal elements, and therefore, some variability in wear behavior among the tested materials is expected. In particular, PPS2MoS_2/CF32f, with a lower content of MoS_2, demonstrates inadequate wear resistance, showing high linear wear rates, and further confirms incomplete or unstable tribofilm formation. In contrast, PPS5MoS_2/CF32f exhibits a favorable performance comparable to the reference material lubricated with PTFE, although this is accompanied by a higher initial wear rate and an extended run-in phase. This behavior suggests that a lower MoS_2 volume fraction requires a greater amount of matrix material to be transferred before a stable tribofilm is established. Once the steady-state friction regime is reached, PPS5MoS_2/CF32f exhibits reduced wear rates compared to the PTFE-based PPS10PTFE/CF32f, confirming the effectiveness of the MoS_2-based lubricating layer. In general, these findings confirm that concentrations of MoS_2 greater than 0.6 vol.% are necessary to achieve optimal tribological performance in PPS matrix composites. The most pronounced differences between formulations occur during the run-in phase, where PPS5MoS_2/CF32f exhibits higher initial wear before reaching stable operation with low friction and wear.

Microstructural analysis of short fiber reinforced PPS with MoS_2 dry lubricant (PPS5MoS_2/CF32f) reveals a distinctive damage evolution compared to the PTFE containing reference material (PPS10PTFE/CF32f). The combined application of LOM, SCT, and DVC techniques provides a comprehensive understanding of the deformation and failure mechanisms governing the response of the composites under axial loading. In the reference material (PPS10PTFE/CF32f), which contains 10 wt.% PTFE, the lubricant phase is distributed throughout the PPS matrix, forming larger particles within the polymer matrix and at the fiber–matrix interfaces. These observations are consistent with previous reports of PTFE dry-lubricants in PI and PPS matrix polymers [24,25,58]. In contrast, the MoS_2 particles in PPS2MoS_2/CF32f and PPS5MoS_2/CF32f show a more homogeneous dispersion, with a particle size largely independent of the lubricant content. Although their aspect ratios are mechanically less favorable, MoS_2 inclusions show minimal accumulation at the fiber–matrix interface, compared to PTFE. Injection molding inherently introduces defects at the phase boundaries caused by the mismatch in thermal expansion coefficients between the composite constituents. During cooling and solidification, micrometer-scale pores can form around both PTFE and MoS_2 particles. These isolated interfacial defects are located mainly at the MoS_2-PPS and PTFE-PPS boundaries. The prevalence of such features indicates that MoS_2 particles act as preferential sites for early void nucleation, driven by weak interfacial adhesion between CF and PPS matrix, as well as localized stress concentrations under load. Under increasing axial loads, the evolution of these initial imperfections depends on the type of dry lubricant. In PPS5MoS_2/CF32f increasing stress levels cause the voids to coalesce and grow, accompanied by the formation of new porosities at the fiber–matrix interface, particularly in regions where fibers are unfavorably oriented relative to the loading direction. The strain localization observed in the DVC fields at 170 N coincides with the onset of interfacial debonding, confirming that these microstructural heterogeneities govern the early stages of damage initiation. At higher loads (200 N), damage accumulation intensifies, characterized by the enlargement of preexisting cracks, nucleation of additional voids and evidence of crack bridging through the PPS matrix indicating limited energy dissipation before catastrophic failure. Although MoS_2 inclusions do not directly alter crack propagation paths, they consistently correlate with localized porosity development, which implies an indirect contribution to fracture mechanics. With increasing load and concurrent activation of manufacturing defects, fiber-end (head) cracking emerges as one of the dominant early failure mechanisms. In short fiber-reinforced polymers, this marks the onset of a well-established

damage sequence: Fiber-end cracking followed by interfacial debonding and subsequent matrix cracking. This progression is consistent with established findings for other short fiber-reinforced polymer systems such as polyamide reinforced with glass fibers (PAGF) [59–61], and is confirmed by the present observations. Comparison with the reference containing PTFE (PPS10PTFE/CF32f) highlights the crucial role of lubricant morphology and interfacial characteristics in defining fracture behavior. In PPS5MoS_2/CF32f, crack propagation is mainly governed by fiber–matrix debonding along the fiber direction, producing a relatively linear crack trajectory. In contrast, PTFE in PPS10PTFE/CF32f promotes local stress concentrations and facilitates initiation of defects and crack bridging. These PTFE particles weaken fiber–matrix adhesion, resulting in larger voids and crack bifurcation, with cracks propagating perpendicular to the loading direction through the matrix. The presence of PTFE also introduces secondary damage mechanisms, producing rougher and more irregular fracture surfaces. DVC analysis confirms a strong correlation between localized strain concentrations and damage nucleation, particularly near PTFE particles, as demonstrated in a previous study [25]. These microstructural interactions account for the observed differences in damage morphology and may contribute to the improved macroscopic strength of PPS5MoS_2/CF32f. The findings underscore how PTFE not only weakens the matrix, but also fundamentally affects the propagation behavior of cracks by altering the reinforcement architecture compared to the MoS_2-lubricated PPS composite. Interfacial debonding along fiber lengths may be challenging to detect, particularly when it is not accompanied by significant void formation or when the interfacial gap falls below the spatial resolution of the imaging system. In general, the results demonstrate that incorporation of MoS_2 alters the micromechanical response of short fiber reinforced PPS by promoting early nucleation of the pores at the particle sites while reducing large-scale interfacial damage compared to systems filled with PTFE. Balancing these competing effects is crucial for optimizing composite formulations intended for hydrogen compressor piston ring applications, where both wear resistance and structural integrity under cyclic loading are essential. Future studies should aim to tailor the dispersion of MoS_2 particles and improve interfacial bonding to maximize the benefits on crack resistance while minimizing porosity formation.

In summary, PPS5MoS_2/CF32f represents the most favorable balance between mechanical stability and tribological performance within the investigated range. At lower concentrations, the formation of a continuous and stable transfer film is insufficient, resulting in elevated friction and excessive wear during the run-in phase. The formulation containing 5 wt.% MoS_2 therefore achieves stable low-friction behavior under hydrogen atmosphere while maintaining compressive strength, dimensional stability, and controlled damage evolution superior to the reference material with 15 wt.% PTFE. This composition can thus be considered a candidate for dry-running piston ring applications in high-pressure hydrogen compressors, while the refinement of the composition is subject to further development.

Finally, the results of this study indicate that MoS_2 is a viable solid lubricant for PPS matrix composites, which exhibits superior tribological performance compared to PTFE under simulated dry-running hydrogen compressor operation conditions. However, the concentration of MoS_2 is a critical optimization parameter. Although sufficient lubricant fractions promote the formation of a stable and efficient transfer layer, low MoS_2 contents do not provide consistent lubrication and lead to unstable friction performance. The run-in phase is particularly affected, as MoS_2-filled composites generally exhibit higher initial wear before reaching steady-state conditions, likely attributed to the smaller volume fraction of lubricating particles compared to PPS10PTFE/CF32f. This elevated run-in wear must therefore be taken into account when designing piston and packing rings to ensure reliable long-term performance under dry-running operation. A low coefficient of friction also makes a significant contribution to reducing frictional heat and is therefore essential for the suitability of polymers in general and PPS matrix composites in particular under high-pressure conditions. According to the data presented, MoS_2 is more suitable for this purpose under hydrogen than PTFE.

It should be noted that piston and packing rings in reciprocating compressors are subjected to complex cyclic loading conditions during service. The present study focuses on the preselection of materials using quasistatic monotonic mechanical testing and tribological investigations to isolate material-specific deformation and damage mechanisms. Long-term durability and cyclic performance under realistic multiaxial stress state experienced in operation, including combined mechanical, thermal, and tribological loading therefore shall be assessed in ongoing compressor endurance tests under realistic operating conditions to confirm their suitability for practical implementation.

CRediT authorship contribution statement

Alexander Pöllinger: Writing – original draft, Visualization, Methodology, Investigation, Conceptualization. **Julia Thalhammer:** Visualization, Investigation, Data curation. **Sarah Heupl:** Visualization, Investigation, Data curation. **Fabian Wilde:** Investigation. **Gábor Szakács:** Investigation. **Stefan Krenn:** Visualization, Investigation, Data curation. **Klaus Gebhardt:** Resources, Investigation. **Eleni Siakkou:** Resources, Investigation. **Thomas Koch:** Investigation. **Vasiliki-Maria Archodoulaki:** Writing – review & editing. **Michael Schöbel:** Writing – review & editing, Supervision.

Declaration of competing interest

The authors declare that they have no known competing financial interests or personal relationships that could have appeared to influence the work reported in this paper.

Acknowledgments

In particular, the authors thank Daniel Hamburger, M.Eng. for his great support, significantly improving the quality of this article.

The authors acknowledge DESY (Hamburg, Germany), a member of the Helmholtz Association HGF, for the provision of experimental facilities. Parts of this research were carried out at PETRA III and the authors thank Fabian Wilde for assistance with the use of Beamline P05. Beamtime was allocated for proposal(s) I-20230472 EC.

The detailed CT-Data evaluations were supported by the projects “Hydrogen Solutions for Optimal Low-carbon Viability and Emissions Control” (HySOLVE) funded by the federal government of Upper Austria and the Just Transition Fund (JTF) in the framework of the EU-Program “IBW-EFRE/JTF 2021–2027” and “IMP4Zero-E: Innovative Monitoring- und Prüfverfahren für den Zero-Emission-Antriebsstrang” (IMP4Zero-E) funded by the Upper Austrian Government.

A significant part of this work was carried out as part of the COMET Center InTribology (FFG no. 906860), a project of the “Excellence Center for Tribology” (AC2T research GmbH). InTribology is funded within the COMET — Competence Centers for Excellent Technologies — Program by the federal ministries BMK and BMAW as well as the federal states of Niederösterreich and Vorarlberg based on financial support from the project partners involved. COMET is managed by The Austrian Research Promotion Agency (FFG). The authors express their gratitude to Andreas Nevosad for his tribological expertise, as well as to Harald Rojacz, Philipp Prettner and Lukas Hönig for their efforts in conducting experiments. The authors also thank Raphael Freiler for his work in evaluating the test data and Tetyana Khmelevska and Markus Premauer for their contributions in measuring and analyzing the 3D topography of the test samples.

The authors acknowledge TU Wien Bibliothek for financial support through its Open Access Funding Programme.

Data availability

Data will be made available on request.

References

[1] Horowitz CA. Paris agreement. Int Leg Mater 2016;55(4):740–55. http://dx.doi.org/10.1017/S0020782900004253.

[2] Sdanghi G, Maranzana G, Celzard A, Fierro V. Review of the current technologies and performances of hydrogen compression for stationary and automotive applications. Renew Sustain Energy Rev 2019;102:150–70. http://dx.doi.org/10.1016/j.rser.2018.11.028.

[3] Kakoulaki G, Kougias I, Taylor N, Dolci F, Moya J, Jäger-Waldau A. Green hydrogen in europe – a regional assessment: Substituting existing production with electrolysis powered by renewables. Energy Convers Manage 2021;228:113649. http://dx.doi.org/10.1016/j.enconman.2020.113649.

[4] Cevahir T, Mehmet AÇ. A study on hydrogen, the clean energy of the future: Hydrogen storage methods. J Energy Storage 2021;40:102676. http://dx.doi.org/10.1016/j.est.2021.102676.

[5] Kovač A, Paranos M, Marciuš D. Hydrogen in energy transition: A review. Int J Hydrog Energy 2021;46(16):10016–35. http://dx.doi.org/10.1016/j.ijhydene.2020.11.256, Hydrogen and Fuel Cells.

[6] Parks G, Boyd R, Cornish J, Remick R. Hydrogen station compression, storage, and dispensing technical status and costs: Systems integration. National Renewable Energy Lab (NREL); 2014, http://dx.doi.org/10.2172/1130621.

[7] Kermani NA, Petrushina I, Nikiforov A, Jensen JO, Rokni M. Corrosion behavior of construction materials for ionic liquid hydrogen compressor. Int J Hydrog Energy 2016;41(38):16688–95. http://dx.doi.org/10.1016/j.ijhydene.2016.06.221.

[8] Yuanlin H, Xiaoying X, Wen W. A new cavity profile for a diaphragm compressor used in hydrogen fueling stations. Int J Hydrog Energy 2017;42(38):24458–69. http://dx.doi.org/10.1016/j.ijhydene.2017.08.058.

[9] Leobersdorfer Maschinenfabrik GmbH. Alternative energy - lmf.at. 2025, URL https://www.lmf.at/applications/alternative-energy/. [Accessed 10 January 2025].

[10] ISO 14687:2025. Hydrogen fuel quality — Product specification. Standard, Geneva, CH: International Organization for Standardization; 2025.

[11] SAE J2719-2020. Hydrogen fuel quality for fuel cell vehicles. Standard, 2020, Warrendale, PA, USA: SAE International; 2020, http://dx.doi.org/10.4271/J2719_202003.

[12] EN 17124:2022. Hydrogen fuel – Product specification and quality assurance for hydrogen refuelling points dispensing gaseous hydrogen – Proton exchange membrane (PEM) fuel cell applications for vehicles. Standard, 2022, Brussels, BE: European Committee for Standardization (CEN); 2022.

[13] Cheng X, Shi Z, Glass N, Zhang L, Zhang J, Song D, sheng Liu Z, Wang H, Shen J. A review of PEM hydrogen fuel cell contamination: Impacts, mechanisms, and mitigation. J Power Sources 2007;165:739–56. http://dx.doi.org/10.1016/j.jpowsour.2006.12.012.

[14] Flitney R. Chapter four - reciprocating seals. In: Flitney R, editor. Seals and sealing handbook (sixth edition). 6th ed.. Oxford: Butterworth-Heinemann; 2014, p. 289–368. http://dx.doi.org/10.1016/B978-0-08-099416-1.00004-8.

[15] Sawae Y, Morita T, Takeda K, Onitsuka S, Kaneuti J, Yamaguchi T, Sugimura J. Friction and wear of PTFE composites with different filler in high purity hydrogen gas. Tribol Int 2021;157:106884. http://dx.doi.org/10.1016/j.triboint.2021.106884.

[16] Çakir M, Akin E. Characterization of carbon fiber-reinforced thermoplastic and thermosetting polyimide matrix composites manufactured by using various synthesized PI precursor resins. Compos B 2022;231:109559. http://dx.doi.org/10.1016/j.compositesb.2021.109559.

[17] Xin D, Feng J, Xu Y, Peng X. Study of the pressure distribution between the piston rings in reciprocating compressors. Adv Mater Res 2011;383–390:6048–52. http://dx.doi.org/10.4028/www.scientific.net/AMR.383-390.6048.

[18] Maer P, Mitchell P, Atkins B. Multi-phase filled-plastics piston rings for non-lubricated compressors: A comparison of the performance of filled ptfe and epoxy-bonded materials in dry gases. Tribology 1973;6(4):129–34. http://dx.doi.org/10.1016/0041-2678(73)90158-9.

[19] Madhan K, Padmanaban R, Venkatesh G. Formulation and numerical investigation of PTFE-based composites for piston rings of oil free air compressors. In: Recent advances in materials technologies. Singapore: Springer Nature Singapore; 2023, p. 87–98. http://dx.doi.org/10.1007/978-981-19-3895-5_7.

[20] Balasaheb W, Abhang LB. Experimental investigation of tribological properties of compressor piston ring with PEEK. Int J Eng Dev Res 2012;8(2):207–16.

[21] Radcliffe C. Sealing material developments for reciprocating gas compressors. Seal Technol 2005;2005(11):7–11. http://dx.doi.org/10.1016/S1350-4789(05)70872-2.

[22] Schelling A, Kausch H, Roulin A. Friction behaviour of polyetheretherketone under dry reciprocating movement. Wear 1991;151(1):129–42. http://dx.doi.org/10.1016/0043-1648(91)90353-V.

[23] Schelling A, Kausch H. Chapter 3 - reciprocating dry friction and wear of short fibre reinforced polymer composites. In: Friedrich K, editor. Advances in composite tribology. Composite materials series, vol. 8, Elsevier; 1993, p. 65–105. http://dx.doi.org/10.1016/B978-0-444-89079-5.50007-6.

[24] Pöllinger A, Maurer J, Koch T, Krenn S, Plank B, Schwarz S, Stöger-Pollach M, Siakkou E, Smrczkova K, Schöbel M. Characterization of PPS piston and packing ring materials for high-pressure hydrogen applications. Polymers 2024;16(3). http://dx.doi.org/10.3390/polym16030412.

[25] Pöllinger A, Maurer J, Heupl S, Wilde F, Tolnai D, Krenn S, Gebhardt K, Siakkou E, Burgstaller C, Archodoulaki V-M, Schöbel M. The effect of PTFE on the deformation behavior of PPS composites for high-pressure hydrogen applications. Compos B 2025. http://dx.doi.org/10.1016/j.compositesb.2025.112692.

[26] Hill Jr HW, Brady DG. Properties, environmental stability, and molding characteristics of polyphenylene sulfide. Polym Eng Sci 1976;16(12):831–5. http://dx.doi.org/10.1002/pen.760161211.

[27] Noll A, Friedrich K, Burkhart T, Breuer U. Effective multifunctionality of poly(p-phenylene sulfide) nanocomposites filled with different amounts of carbon nanotubes, graphite, and short carbon fibers. Polym Compos 2013;34(9):1405–12. http://dx.doi.org/10.1002/pc.22427.

[28] Lopes de Oliveira MC, Sayeg IJ, Ett G, Antunes RA. Corrosion behavior of polyphenylene sulfide–carbon black–graphite composites for bipolar plates of polymer electrolyte membrane fuel cells. Int J Hydrog Energy 2014;39(29):16405–18. http://dx.doi.org/10.1016/j.ijhydene.2014.07.175.

[29] Huang J, Baird DG, McGrath JE. Development of fuel cell bipolar plates from graphite filled wet-lay thermoplastic composite materials. J Power Sources 2005;150:110–9. http://dx.doi.org/10.1016/j.jpowsour.2005.02.074.

[30] Hoadley J, Ginter J. Polyphenylene sulfide (PPS) as a membrane in electrolysis cells. In: 26th international conference on environmental systems. United States: SAE International; 1996, p. 1–7.

[31] Lopez LC, Wilkes GL. Poly(p-phenylene sulfide) — An overview of an important engineering thermoplastic. J Macromol Sci C 1989;29(1):83–151. http://dx.doi.org/10.1080/07366578908055165.

[32] Moran K, Lake P, Dole J. Using polyphenylene sulphide in high-performance pumps. World Pumps 2002;2002(434):27–31. http://dx.doi.org/10.1016/S0262-1762(02)80264-4.

[33] Ning H, Vaidya U, Janowski GM, Husman G. Design, manufacture and analysis of a thermoplastic composite frame structure for mass transit. Compos Struct 2007;80(1):105–16. http://dx.doi.org/10.1016/j.compstruct.2006.04.036.

[34] Yu L, Bahadur S. An investigation of the transfer film characteristics and the tribological behaviors of polyphenylene sulfide composites in sliding against tool steel. Wear 1998;214(2):245–51. http://dx.doi.org/10.1016/S0043-1648(97)00234-2.

[35] Zhao Q, Bahadur S. A study of the modification of the friction and wear behavior of polyphenylene sulfide by particulate Ag2S and PbTe fillers. Wear 1998;217(1):62–72. http://dx.doi.org/10.1016/S0043-1648(98)00155-0.

[36] Han Y, Schmitt S, Friedrich K. Microfriction studies of filled PPS/PTFE-composite blends. Ind Lubr Tribol 2001;53(1):32–43. http://dx.doi.org/10.1108/00368790110366406.

[37] Chen Z, Liu X, Lü R, Li T. Mechanical and tribological properties of PA66/PPS blend. III. reinforced with GF. J Appl Polym Sci 2006;102(1):523–9. http://dx.doi.org/10.1002/app.24253.

[38] Blanchet TA, Kennedy FE. Sliding wear mechanism of polytetrafluoroethylene (PTFE) and PTFE composites. Wear 1992;153:229–43. http://dx.doi.org/10.1016/0043-1648(92)90271-9.

[39] Schöbel M, Langela M, Koch T, Pöllinger A. High-strength PPS-polymer composites for hydrogen high-pressure applications. In: Key engineering materials. vol. 967, 2023, p. 3–9. http://dx.doi.org/10.4028/p-3b1yxv.

[40] Winkelmann H, Pöllinger A, Bernardi J, Whitmore K, Schwarz S, Krenn S, Seichter S, Schöbel M. Wear mechanisms and material deposition of high-performance polymer composites for hydrogen compression. Eng Fail Anal 2024;164:108712. http://dx.doi.org/10.1016/j.engfailanal.2024.108712.

[41] The European Commission. Chemicals strategy for sustainability towards a toxic-free environment. Tech. rep. 247–268, European Union: Directorate-General for Environment; 2020, http://dx.doi.org/10.1007/s42114-018-0023-8, URL https://eur-lex.europa.eu/legal-content/EN/ALL/?uri=COM:2020:667:FIN.

[42] Feldman J. Elastic constants of 2H-mos2 and 2H-nbse2 extracted from measured dispersion curves and linear compressibilities. J Phys Chem Solids 1976;37(12):1141–4. http://dx.doi.org/10.1016/0022-3697(76)90143-8.

[43] Dhanumalayan E, Joshi GM. Performance properties and applications of polytetrafluoroethylene (PTFE)—a review. Adv Compos Hybrid Mater 2018;1(2):247–68. http://dx.doi.org/10.1007/s42114-018-0023-8.

[44] voestalpine BÖHLER Edelstahl GmbH & Co KG. W360 ISOBLOC - böhler edelstahl gmbh & co KG. 2024, URL https://www.bohler-edelstahl.com/de/products/w360-isobloc/. [Accessed 10 January 2025].

[45] Moosmann J, Wieland DCF, Zeller-Plumhoff B, Galli S, Krüger D, Ershov A, Lautner S, Sartori J, Dean M, Köhring S, Burmester H, Dose T, Peruzzi N, Wennerberg A, Willumeit-Römer R, Wilde F, Heuser P, Hammel JU, Beckmann F. A load frame for in situ tomography at PETRA III. In: Müller B, Wang G, editors. Developments in x-ray tomography XII. vol. 11113, SPIE, International Society for Optics and Photonics; 2019, 1111318. http://dx.doi.org/10.1117/12.2530445.

[46] Maurer J, Salaberger D, Jerabek M, Kastner J, Major Z. Quantitative investigation of local strain and defect formation in short glass fibre reinforced polymers using X-ray computed tomography. Nondestruct Test Eval 2022;37(5):582–600. http://dx.doi.org/10.1080/10589759.2022.2075865.

[47] Moosmann J, Ershov A, Weinhardt V, Baumbach T, Prasad MS, LaBonne C, Xiao X, Kashef J, Hofmann R. Time-lapse X-ray phase-contrast microtomography for in vivo imaging and analysis of morphogenesis. Nat Protoc 2014;9(2):294–304. http://dx.doi.org/10.1038/nprot.2014.033.

[48] Hori M, Fujimoto K, Hori T, Sekine H, Ueno A, Kato A, Kawai T. Development of image analysis using python: Relationship between matrix ratio of composite resin and curing temperature. Dent Mater J 2020;39(4):648–56. http://dx.doi.org/10.4012/dmj.2019-163.

[49] Galos J, Wang X. Demonstration of computer vision for void characterisation of 3D-printed continuous carbon fibre composites. Results Mater 2024;22:100566. http://dx.doi.org/10.1016/j.rinma.2024.100566.

[50] Otsu N. A threshold selection method from gray-level histograms. IEEE Trans Syst Man Cybern 1979;9(1):62–6. http://dx.doi.org/10.1109/TSMC.1979.4310076.

[51] ISO 6721-7:2019. Determination of dynamic mechanical properties - Part 7: Torsional vibration — Non-resonance method. Standard, Geneva, CH: International Organization for Standardization; 2019.

[52] ISO 11359-2:2021. Plastics — Thermomechanical analysis (TMA) - Part 2: Determination of coefficient of linear thermal expansion and glass transition temperature. Standard, Geneva, CH: International Organization for Standardization; 2021.

[53] ISO 527-2:2012. Plastics — Determination of tensile properties - Part 2: Test conditions for moulding and extrusion plastics. Standard, Geneva, CH: International Organization for Standardization; 2012.

[54] ISO 604:2022. Plastics — Determination of compressive properties. Standard, Geneva, CH: International Organization for Standardization; 2022.

[55] Rebenfeld L, Desio GP, Wu JC. Effects of fibers on the glass transition temperature of polyphenylene sulfide composites. J Appl Polym Sci 1991;42(3):801–5. http://dx.doi.org/10.1002/app.1991.070420324.

[56] Golzar M, Sinke J, Abouhamzeh M. Novel thermomechanical characterization for shrinkage evolution of unidirectional semi-crystalline thermoplastic prepregs (PPS/CF) in melt, rubbery and glassy states. Compos A 2022;156:106879. http://dx.doi.org/10.1016/j.compositesa.2022.106879.

[57] Nath RB, Fenner DN, Galiotis C. Finite element modelling of interfacial failure in model carbon fibre-epoxy composites. J Mater Sci 1996;31(11):2879–83. http://dx.doi.org/10.1007/BF0355996.

[58] Pöllinger A, Koch T, Krenn S, Wilde F, Tolnai D, Plank B, Heupl S, Bernardi J, Whitmore K, Langela M, Seichter S, Schöbel M. Thermo-mechanical properties and internal architecture of PI composites for high-pressure hydrogen applications. Polymer 2023;289:126500. http://dx.doi.org/10.1016/j.polymer.2023.126500.

[59] Sato N, Kurachi T, Sato S, Kamigaito O. Mechanism of fracture of short glass fibre-reinforced polyamide thermoplastic. J Mater Sci 1984;19(4):100566. http://dx.doi.org/10.1007/BF01120023.

[60] Arif M, Saintier N, Meraghni F, Fitoussi J, Chemisky Y, Robert G. Multiscale fatigue damage characterization in short glass fiber reinforced polyamide-66. Compos B 2014;61:55–65. http://dx.doi.org/10.1016/j.compositesb.2014.01.019.

[61] Belmonte E, De Monte M, Hoffmann C-J, Quaresimin M. Damage mechanisms in a short glass fiber reinforced polyamide under fatigue loading. Int J Fatigue 2017;94:145–57. http://dx.doi.org/10.1016/j.ijfatigue.2016.09.008.